Publications:

Research papers

- Pathania K, Sah SP, Salunke DB, Jain M, Yadav AK, Yadav VG, Pawar SV. Green synthesis of lignin-based nanoparticles as a bio-carrier for targeted delivery in cancer therapy. Int J Biol Macromol. 2023 Feb 28;229:684-695.
- Pothal, P, Pathania, K., Kumar, S, Kaur, J, Sah, S. P, Singh, R, & Pawar, S. V. Lignin-chitosan biocomposite film for antimicrobial activity: Fabrication, characterization and in-vitro evaluation. Materials Letters, 2023 133956.
- V. Mutreja, A. Kumar, S. Sareen, K. Pathania, H. Sandhu, R. Kataria, S. V. Pawar, S. K. Mehta, J. Park, ChemistrySelect 2022, 7, e202200448. Aggregation-Induced Quenching of Carbon Dots for Detection of Nitric oxide
- D Kaushik, M Kaur, V Mutreja, K Pathania, DB Salunke, SC Sahoo, V. Saini, SV Pawar, SK Kansal, SK Mehta. Synthesis of quinoline based molecular probes for detection of nitric oxide Dyes and Pigments, 110226
- S Sharma, A Kaur, S Kumar, K Pathania, K Kumar, R Arora, S.K Mehta, et al. 2023. "Lignin Nanoparticles as a Novel Carrier for Efficacious Delivery of Toll like Receptor 7/8 Agonist: Physicochemical and In-Vitro Evaluation." Journal of the Indian Chemical Society 100 (5): 101008–8. https://doi.org/10.1016/j.jics.2023.101008.

Review papers

- Mukheja, Y., Kaur, J., Pathania, K., Sah, S. P., Salunke, D. B., Sangamwar, A. T., & Pawar, S. V. (2023). Recent advances in pharmaceutical and biotechnological applications of lignin-based materials. International Journal of Biological Macromolecules, 124601.
- J Garg, K Pathania, SP Sah, SV Pawar. Nanostructured lipid carriers: a promising drug carrier for targeting brain tumours. Future Journal of Pharmaceutical Sciences 8 (25), 1-31

Book chapters

- Brain tumor: an insight into in-vitro and in-vivo experimental models (Book Chapter, Bentham Science Publishers) K Pathania, S Sharma, SV Pawar and SP Sah.
- In-vitro models of age-related neurodegenerative diseases (Book Chapter, Bentham Science Publishers) S Sharma, K Pathania, SP Sah and SV Pawar.

International Journal of Biological Macromolecules 229 (2023) 684–695

Contents lists available at ScienceDirect

International Journal of Biological Macromolecules

journal homepage: www.elsevier.com/locate/ijbiomac

Green synthesis of lignin-based nanoparticles as a bio-carrier for targeted delivery in cancer therapy

Khushboo Pathania [a], Sangeeta P. Sah [a], Deepak B. Salunke [b,c], Manish Jain [a], Ashok Kumar Yadav [a], Vikramaditya G. Yadav [d,e], Sandip V. Pawar [a,*]

[a] University Institute of Pharmaceutical Sciences, Panjab University, Chandigarh, India
[b] Department of Chemistry and Centre of Advanced Studies, Panjab University, Chandigarh, India
[c] National Interdisciplinary Centre of Vaccine, Immunotherapeutics & Antimicrobials, Panjab University, Chandigarh, India
[d] Department of Chemical and Biological Engineering, The University of British Columbia, Vancouver, BC, Canada
[e] School of Biomedical Engineering, The University of British Columbia, Vancouver, BC, Canada

ARTICLE INFO

Keywords:
Lignin
Biovalorization
Magnetic nanoparticles
Chemotherapy
Targeted drug delivery
Theranostics

ABSTRACT

Polymeric magnetic nanoparticles have shown higher efficacy in cancer diagnosis and treatment than conventional chemotherapies. Lignin is an abundantly available natural polymer that can be selectively modified using a rapidly expanding toolkit of biocatalytic and chemical reactions to yield 'intelligent' theranostic-nanoprobes. We aim to valorize lignin to develop a natural polymeric-magnetic-nano-system for the targeted delivery of methotrexate. In the current study, we synthesized nanoparticles of lignin and iron oxide with methotrexate using a new approach of anti-solvent precipitation with ultrasonication. The ensuing nanoparticles are magnetic, smooth, polyhedral with characteristic dimension of 110-130 nm. The drug loading and encapsulation efficiencies were calculated to be 66.06 % and 64.88 %, respectively. The nanoparticles exhibit a concentration-dependent release of methotrexate for the initial 24 h, followed by sustained release. Moreover, formulation is non-hemolytic and scavenges radicals owing to the antioxidant property of lignin. Additionally, methotrexate delivered using the nanoparticles exhibited higher cytotoxicity in cellular-viability assays employing breast cancer and macrophage cell lines compared to the pure form of the drug. Synergistic action of lignin, iron oxide, and methotrexate contribute to enhanced caspase-3 activity and reduced glutathione levels in the breast cancer cells, as well as elevated internalization of the drug on account of increased receptor-mediated endocytosis.

1. Introduction

Cancer afflicts nearly 20 million individuals each year [1]. The disease is characterized by uncontrolled cellular growth and can rapidly spread to other parts of the body if left unchecked. Although chemotherapy continues to be the first line of defense against numerous cancers, the treatment suffers from several limitations. Chemotherapy is poorly specific and usually causes adverse side effects. Moreover, the drug molecules are not very soluble in biofluids and cancers eventually develop resistance to the treatment [2]. Nanomedicines directly address these shortcomings and can improve the stability, solubility, and circulating half-life of the drug compound [3]. In fact, the unique pathophysiology of tumor cells and their microenvironment, including leaky vasculature and dysfunctional lymphatic drainage, play to the strengths of nanomedicines. Since its discovery about 30 years ago, the enhanced permeability and retention (EPR) effect has become the guiding principle for cancer nanomedicine development. The aberrant pathophysiology like leaky vasculature enables nanoparticles to specifically accumulate inside the tumor cells. Furthermore, the dysfunctional lymphatic drainage in tumors retains the accumulated nanocarriers and allows them to release drugs into the vicinity of the tumor cells [4,5]. Experimental studies suggest that the threshold size for extravasation into tumors is ~400 nm, with best results reported with size<200 nm [6]. This higher accumulation of nanoparticles in tumor tissue than in healthy tissues is called passive targeting. When passive targeting of tumors proves to be insufficient, nanoparticles can also be chemically modified or conjugated with targeting ligands such as antibodies to stimulate targeted delivery [7]. Magnetization through the inclusion of iron oxide is one of the most common approaches to actively target nanoparticles to their intended site of action, and magnetic

* Corresponding author at: University Institute of Pharmaceutical Sciences, Panjab University, Chandigarh 160014, India.
E-mail address: pawars@pu.ac.in (S.V. Pawar).

https://doi.org/10.1016/j.ijbiomac.2022.12.323
Received 1 October 2022; Received in revised form 12 December 2022; Accepted 28 December 2022
Available online 2 January 2023

nanoparticles have been employed as theranostic systems, drug delivery vehicles, bioimaging contrast agents, and nutritional supplements for the treatment of anemia [8]. However, the accumulation of iron oxide within cells can catalyze the formation of reactive oxygen species (ROS), which can elicit cytotoxic effects on account of oxidative stress [9]. Bare nanoparticles of iron oxide are also susceptible to aggregation and degrade rapidly *in vivo* [10].

Coating magnetic iron oxide nanoparticles with a biocompatible polymer offer a compelling solution for active targeting of tumors that overcomes all foreseeable limitations of bare nanoparticles. To this end, lignin is a highly promising candidate. It is abundant, non-toxic, biodegradable, and cheap [11,12], and its uniquely branched structure that is suffused with functional groups makes it amenable to facile chemical modification [13–15]. In the current study, we synthesized magnetic nanoparticles of iron oxide and coated them using lignin. We subsequently conjugated the coated particles to methotrexate (MTX), an anti-metabolite drug that elicits anti-cancer activity through antagonism of folic acid metabolism by two previously reported methods and a new approach. Like most potent chemotherapeutic agents, MTX is poorly soluble in water, distributes non-specifically, adsorbs variably in tissues, has a short circulation half-life, is nephro- and hepatotoxic and loses efficacy over time owing to development of resistance [16]. The synthesized magnetic nanoparticles were further evaluated for successful formation of nanohybrids using various physicochemical characteristics like size, shape, pH, zeta potential, thermal characteristics, magnetic behaviour, drug loading, and release profile. The prepared nanoparticles were screened for their hemo-compatibility and antioxidant potential. The cytotoxicity was studied in breast cancer, cervical cancer, and murine macrophage cell lines. Also, in breast cancer cells, the cellular uptake is visualized along with the levels of cytotoxicity and apoptotic markers like caspase-3, glutathione, and DNA fragmentation with nuclear condensation. Additionally, the nanoformulation was tested for its stability profile over a period of 12 months.

2. Experimental

2.1. Chemicals, reagents and cells

Alkali lignin (AL) was purchased from Sigma-Aldrich India. Methotrexate hydrate was purchased from Tokyo Chemical Industry. Ferric chloride hexahydrate, ferrous sulfate heptahydrate, and dimeythyl sulfoxide (DMSO) were purchased from Thermo Fischer Scientific India. Dulbecco's Modified Eagle's Medium (DMEM) and streptomycin-penicillin were purchased from Lonza. 2,2-Diphenyl-1-picryl hydrazyl (DPPH), Roswell Park Memorial Institute 1640 medium (RPMI 1640), fetal bovine serum (FBS) and phosphate-buffered saline (PBS) were purchased from HiMedia India. FITC and NP 40 lysis buffer were purchased from Invitrogen and protease inhibitor cocktail was purchased from Genetix Biotech. We obtained RAW 264.7 murine macrophage, HeLa human cervical cancer, and MDA-MB-231 human breast cancer cell lines from the National Center for Cell Science (NCCS, Pune, India). The HeLa cells were cultured in RPMI 1640, whereas the RAW and breast cancer cells were maintained in DMEM. Both media were supplemented with 10 % FBS and 1 % penicillin-streptomycin and the cultures were incubated at 37 °C in a humidified 5 % CO_2–95 % air atmosphere.

2.2. Synthesis of iron oxide nanoparticles

We used chemical co-precipitation to synthesize iron oxide [17]. We initially dissolved ferric chloride hexahydrate and ferrous sulfate heptahydrate in deionized water to final concentrations of 0.1 M each and purged both solutions with nitrogen. We then combined the solutions (1:1 M) in a two-necked, round-bottom flask and magnetically stirred the mixture at 60 °C under nitrogen for 30 min. We then added a 10 wt% ammonia solution to the mixing solution in a dropwise manner until the pH of the solution reached 10 while gradually raising the temperature to 90 °C. The solution changed from orange to black and the stirring was maintained for another 2 h at 90 °C. We then centrifuged the contents of the flask at 7000 rpm for 10 min and washed the precipitate three times with distilled water to remove any excess ammonia. We later collected the iron oxide nanoparticles using a strong magnet and dried them overnight at 80 °C.

2.3. Preparation of lignin-coated nanoparticle

We prepared a solution of 0.5 mg/mL lignin and iron oxide in deionized water and 1 mg/mL MTX in DMSO and subsequently used three different approaches, namely *in situ* addition [17], self-assembly using vortex [18] and a new modified approach of anti-solvent precipitation with ultrasonication [19], to synthesize the lignin-coated iron oxide nanoparticles. *In situ* addition proceeded with the dropwise addition of the lignin solution to the iron oxide solution, followed by vigorous stirring for 8 h to yield the lignin-coated iron oxide nanoparticles (LIONs). In a parallel step, lignin and drug solutions were added dropwise and simultaneously to the iron oxide solution and then stirred for 8 h to produce drug-loaded, lignin-coated nanoparticles. Since the physicochemical properties of the formulation are influenced greatly by the drug-to-polymer ratio, we varied the volumetric amounts/concentrations of the drug and lignin solutions added to the iron oxide solution and evaluated the influence of this parameter on size, drug loading, and encapsulation efficiency. Anti-solvent precipitation method was employed coupled with ultrasonication technique for preparation of blank and drug-loaded nanoparticles. Lignin solution was added to iron oxide solution under sonication with a bath sonicator and sonication was maintained for 1 h at room temperature (maintained by the addition of cold water as required) to yield LIONs. Similarly, lignin and MTX solutions were added to iron oxide solution under sonication and sonication was maintained for 1 h at room temperature to yield drug-loaded nanoparticles. On the other hand, the vortex method tries to exploit self-assembly and proceeds with the dropwise addition of iron oxide solution to the lignin solution, followed by vortexing for 30 min to produce LIONs. The drug is subsequently loaded by dropwise addition of MTX to the LION solution. We then isolated the nanoparticles by centrifuging the mixtures at 7000 ×g for 10 min and later washing the precipitate three times with distilled water in order to remove non-complexed, excess ingredients. We later collected the nanoparticles using a strong magnet and subsequently lyophilized. All methods yielded nanoparticles of comparable physical and chemical characteristics for similar operational parameters.

2.4. Fluorescent labeling of the nanoparticles

Cellular uptake of the nanoparticles was evaluated through fluorescent labeling. The labeled-nanoparticles were prepared using anti-solvent precipitation with ultrasonication as described in previous section. We introduced 5 mg/mL solution of FITC in DMSO either individually (for blank nanoparticles) or in combination with the MTX solution (for drug-loaded nanoparticles) to the LION mixture under sonication and sonicated it for 1 h at room temperature. We repeated the centrifugation and washing steps and then collected the nanoparticles using a strong magnet. The particles were then lyophilized.

2.5. Measurements of physical characteristics of the nanoparticles

We employed a Nano-ZS Zeta Sizer manufactured by Malvern Instruments to measure the particle size distribution and zeta potentials of the nanoparticles. The particles were suspended in deionized water along with a commercial dispersing agent in a polystyrene cuvette and exposed to a laser at an angle of 90°. We made three recordings and ensured that they are sufficiently apart in time. We also recorded the Fourier-transform infrared (FTIR) spectra and differential scanning

calorimetry (DSC) thermograms of iron oxide, lignin, MTX, LIONs, and drug-loaded nanoparticles. The FTIR spectra were recorded using a PerkinElmer Spectrum Two spectrometer, whereas we used a Waters Q20 TA calorimeter for the DSC measurements. We also performed high-resolution transmission electron microscopy (HRTEM) and field emission scanning electron microscopy (FESEM) using a JEM 2100 Plus electron microscope (JEOL) and scanning electron microscopy using a SU8010 electron microscope (Hitachi) to study the surface morphology of the nanoparticles. We also measured the pH of 1 mg/mL suspension of LIONs in distilled water and also examined the same under an external magnetic field.

2.6. Assessment of the antioxidant activity of the nanoparticles

We measured the antioxidant activity of the nanoparticles using the DPPH assay. Briefly, DPPH forms a free radical in solution, thereby rendering the solution purple. The free radical is subsequently scavenged by hydrogen donors and forms a yellow-colored species. The greater a substance's antioxidant property, the higher is the scavenging activity in the solution. Consequently, each assay mixture comprises 2 mL of 0.1 mM solution of DPPH in ethanol and 2 mL of the test sample. Ascorbic acid, a potent antioxidant, serves as the positive control and solution without sample taken as negative control. The assay is performed at 37 °C for 30 min in test tubes and the absorbance is measured at 517 nm using UV–Vis spectrophotometer. The antioxidant properties or DPPH radical scavenging activity (RSA) of a substance are then quantified using Eq. (1). RSA is a measure of the antioxidant's inhibition of the protonation of DPPH to form hydrazine.

$$\mathrm{RSA} = \frac{(\text{Absorbance of negative control}) - (\text{Absorbance of the sample})}{(\text{Absorbance of negative control})} \times 100 \tag{1}$$

We plotted the RSA against DPPH concentrations and determined the IC_{50} values for the nanoparticles. The IC_{50} value denotes the concentration of nanoparticles that is needed to scavenge 50 % of the DPPH radicals in solution.

2.7. Calculation of drug loading and encapsulation efficiencies

The drug loading capacity (DLC) is defined as the ratio of the weight of drug that is loaded into the nanoparticle to the weight of the entire nanoparticle. On the other hand, encapsulation efficiency (EE) is defined as the ratio of the weight of drug that is loaded into the nanoparticle to the total weight of the drug that was added into the assembly mixture. We estimated DLC and EE for the nanoparticles using direct as well as indirect approaches. In the direct method, synthesized nanoparticles were initially weighed, then solvated in DMSO, and later sonicated to release the drug into the solvent [20]. We then estimated the concentration of MTX by measuring the UV–Vis absorbance of the solution at 303 nm. In the case of the indirect method, we estimated the concentration of free or unloaded drug in the supernatant that is produced after centrifugation [21]. We performed both sets of measurements on three different samples and reported the DLC and EE as the average of the six recordings.

2.8. Determination of release kinetics and stability of the nanoparticles

We introduced the drug-loaded nanoparticles into dialysis bags having an 8 kDa molecular weight cut-off. The bags were then suspended in 25 mL of phosphate-buffered saline (PBS). We estimated the release kinetics at pH conditions of 6.3 and 7.4. The solutions were maintained at 37 °C and gently agitated at 100 rpm. We frequently sampled the bulk PBS phase at pre-determined intervals. Sampling frequency was higher at the start of the experiment in order to accurately record the initial burst-release of the drug owing to the highly favorable chemical potential gradient at initial time points. We withdrew 2 mL at each sampling point and replaced 2 mL of fresh media to maintain the sink conditions. We estimated the concentrations of MTX in the samples by measuring the UV–Vis absorbance of the solution at 303 nm. We also adjusted the concentrations for dilution due to addition of fresh media. We subsequently analyzed the concentration-time data using the software package DD Solver. We fitted the data to numerous models, including zero-order, first-order, Higuchi, Weibull, and the Korsmeyer-Pappas models. The software package also estimates the rate constants and correlation coefficients for the models. Finally, we evaluated the stability of the formulation by estimating the size and drug content of the nanoparticles at 0, 6, and 12 months under storage at 4 °C.

2.9. Hematoxicity measurements

We evaluated the toxicity of the nanoparticles by studying their effect on red blood cells (RBCs) using a standard hemolysis assay. We collected 4 mL of whole rat blood and transferred the samples to EDTA to prevent coagulation. We then separated the RBCs from the samples by centrifugation at 1500 rpm for 10 min at 4 °C and subsequently washed the purified cells using ice-cold PBS. We repeated the washing and centrifugation steps numerous times until the cell suspension was clear. We subsequently mixed 20 μL of varying concentrations of LIONs, MTX, and the drug-loaded nanoparticles with 180 μL of the RBC suspension and incubated the mixtures at 37 °C for 1 h under constant shaking. PBS solution and 1 % Triton X-100 were used as negative and positive control, respectively. Following incubation, we centrifuged the samples at 1500 rpm for 10 min at 4 °C. The supernatant was collected and analyzed at 540 nm using a BioRad ELISA plate-based spectrophotometer. Hemolysis was quantified as:

$$\%Hemolysis = \frac{(Absorbance\ of\ sample) - (Absorbance\ of\ saline\ mixture)}{(Absorbance\ of\ Triton\ mixture) - (Absorbance\ of\ saline\ mixture)} \times 100 \tag{2}$$

2.10. Cytotoxicity measurements

We employed the colorimetric MTT assay to assess the cytotoxicity of the formulations [22,23]. Briefly, we seeded RAW 264.7 murine macrophage, HeLa human cervical cancer, and MDA-MB-231 human breast cancer cells in individual wells of a 96-well culture plate containing 180 μL of each cell line's specific culture medium. We also individually added varying concentrations of MTX, LIONs, and the drug-loaded nanoparticles to the wells. Control samples did not contain any drug or nanoparticles and blank samples did not contain any cells. The seeding density translated to 5×10^3 cells in each well and the cultures were incubated at 37 °C in an atmosphere comprising 5 % CO_2. Following 24 h of incubation, we replaced the supernatant in each well with fresh medium comprising 5 mg/mL of 3-(4,5-dimethylthiazol-2-yl)-2,5-diphenyltetrazolium bromide (MTT). The cultures were then incubated at 37 °C for an additional 4 h. We subsequently measured the absorbance of each well at 595 nm. The absorbance of blank and control wells was assumed to be 0 % and 100 % viable, respectively, and we used this calibration curve to determine the viability of cells in all the wells. We thereafter determined the IC_{50} values of the drug, LIONs or drug-loaded nanoparticles GraphPad Prism's in-built function by plotting the viability against concentration.

2.11. Estimation of cellular activity

We also quantified the glutathione levels and caspase-3 activity of treated and untreated MDA-MB-231 cells. We initially seeded the cells in a 24-well plate at a density of 5×10^6 cells/well and treated them either with LIONs, MTX, or drug-loaded nanoparticles at two concentrations

(IC_{50} values of MTX and drug-loaded nanoparticles). The cultures were incubated at 37 °C in a humidified incubator supplied with 5 % CO_2. After 24 h had elapsed, we washed the cultures with ice-cold PBS and then treated the cultures with trypsin to detach them from the surface. We subsequently centrifuged the cell suspensions at 1500 rpm for 10 min at room temperature to separate the supernatant and then lysed the cells with 10× NP-40 buffer supplemented with protease inhibitors. Glutathione (GSH) metabolism in the cells was quantified by supplying 5,5′-dithio-bis(2-nitrobenzoic acid) (DTNB) to the lysates. DTNB reacts with GSH to produce a yellow-colored derivative 5′-thio-2-nitrobenzoic acid (TNB) that can be detected at 412 nm [24]. The decrease in GSH is determined using:

$$\%\text{Decrease in GSH} = \frac{(\text{Absorbance of sample}) - (\text{Absorbance of control})}{(\text{Absorbance of control})} \times 100 \quad (3)$$

Likewise, caspase-3 activity in the MDA-MB-231 lysates was determined using the GENLISA™ assay kit. The assay involves use of a biotinylated CASP3 antibody to bind caspase-3, followed by treatment using a streptavidin-horseradish peroxidase (HRP) conjugate and incubation at 37 °C for 1 h. The mixtures were washed 4 times using the solution provided in the kit and the blotting substrates 3,3′,5,5′-tetramethylbenzidine (TMB) A and B were later added. A second incubation at 37 °C for 10 min followed suit, after which the stop solution was added to the samples. Absorbance of the samples was detected at 450 nm and the relative increase in caspase-3 activity was determined as:

$$\%\text{Increase in activity} = \frac{(\text{Absorbance of sample}) - (\text{Absorbance of control})}{(\text{Absorbance of control})} \times 100 \quad (4)$$

2.12. Cellular uptake of nanoparticles

We also estimated the uptake of blank and drug-loaded nanoparticles by MDA-MB-231 cells. We seeded the cells on a coverslip in a 6-well plate at a density of 2×10^4 cells/well and allowed the cells to attach by incubating the cultures for 24 h at 37 °C in a 5 % CO_2 atmosphere. The cells were then treated with FITC-labeled blank and drug-loaded nanoparticles and incubated for an additional 4 h. We then washed the cells three times with ice-cold PBS and later fixed the cells with 4 % paraformaldehyde. The fixed cells were counterstained with a 10 μg/mL solution of Hoechst dye and washed a further three times with ice-cold PBS. The mounted cells were then investigated using a Nikon C2 laser-scanning confocal microscope (excitation and emission wavelengths of 352 and 450 nm, respectively [25]) to determine the uptake of the nanoparticles.

2.13. Identification of apoptosis

We probed potential apoptosis using nuclear condensation and DNA fragmentation. To this end, we employed Hoechst 33342 staining. Untreated and treated cells (MTX, LIONs, and drug-loaded nanoparticles) were incubated with a 10 μg/mL solution of Hoechst dye for 5 min, followed by visual analysis using a Nikon C2 laser-scanning confocal microscope under excitation and emission wavelengths of 352 and 450 nm, respectively [25].

2.14. Statistical analysis

All experiments were performed at least three times. All data presented hereinafter is reported as the mean ± standard deviation (SD). A p-value of <0.05 was considered to be statistically significant. Statistical analysis was performed using the GraphPad Prism using $^*p < 0.05$, $^{**}p < 0.01$ $^{***}p < 0.001$, and $^{****}p < 0.0001$.

Table 1
Effect of different techniques on particle size and polydispersity index (PDI).

	Average particle size (nm)	PDI
In situ addition	350.7 ± 12	0.328 ± 0.034
Self-assembly using vortex	462.3 ± 20	0.434 ± 0.024
Anti-solvent precipitation with ultrasonication	153.3 ± 3.2	0.182 ± 0.017

Table 2
Characterization of different LION:MTX ratios.

Weight ratio of Lignin:MTX	Encapsulation efficiency (%)	Drug loading (%)	Particle size (nm)	PDI
1:1	64.84 ± 0.19	32.42 ± 0.17	158.9 ± 1.3	0.242 ± 0.047
1:2	64.85 ± 0.17	56.46 ± 0.14	139.4 ± 3.4	0.248 ± 0.048
1:3	64.88 ± 0.14	66.06 ± 0.18	111.85 ± 3.75	0.233 ± 0.054

3. Results and discussion

3.1. Selection of synthesis technique and optimization of drug loading

We investigated 3 different approaches to synthesizing the lignin-iron oxide nanoparticles, namely *in situ* addition, self-assembly using vortex, and a new approach of anti-solvent precipitation with ultrasonication. Analysis of the particle size distribution and polydispersity index (PDI) using dynamic light scattering (DLS) revealed that anti-solvent precipitation with ultrasonication yielded the smallest and least polydisperse particles (Table 1) whereas the particle size with the other two methods was more than the required for passive targeting of tumor. Therefore, we proceeded with the new approach for green synthesis of lignin-based nanoparticles.

Next, we deduced the optimal drug loading for the nanoparticles by varying the weight ratios of MTX and the LIONs (Table 2). The drug-nanoparticle ratio clearly influenced drug loading, particle size, and PDI of the system. However, encapsulation efficiency did not vary. The diminishment in particle size with increasing drug loading is hypothesized to occur owing to an increase in hydrophobic interactions between the drug and aromatic groups in lignin. We selected a 1:3 LION:MTX ratio for subsequent testing in light of the ideal particle size and PDI. The 1:3 LION:MTX nanoparticles are hereinafter simply referred to as drug-loaded nanoparticles.

3.2. Characterization of nanoparticles

3.2.1. Physical properties of the nanoparticles

We estimated the hydrodynamic diameters of the LIONs and drug-loaded nanoparticles using DLS to be 110.65 ± 1.95 nm and 111.85 ± 3.75 nm, respectively. The corresponding PDIs were determined to be 0.2305 ± 0.0485 and 0.233 ± 0.054, respectively (Table 2). The size of the drug-loaded nanoparticles falls within the 20–200 nm range that has been reported to be conducive for passive targeting of tumors and longer residence times owing to slower clear-out from the kidneys, liver, and spleen. Additionally, the PDI of 0.233 for the drug-loaded nanoparticles is indicative of uniform size and moderate polydispersity, which is desirable for efficient drug delivery. Nanoparticles with PDIs that exceed 0.5 have been reported to agglomerate *in vivo*, which conspires to increase particle size and reduce magnetization, thereby negatively impacting delivery of the nanoparticles to the site of action and their uptake thereafter [26].

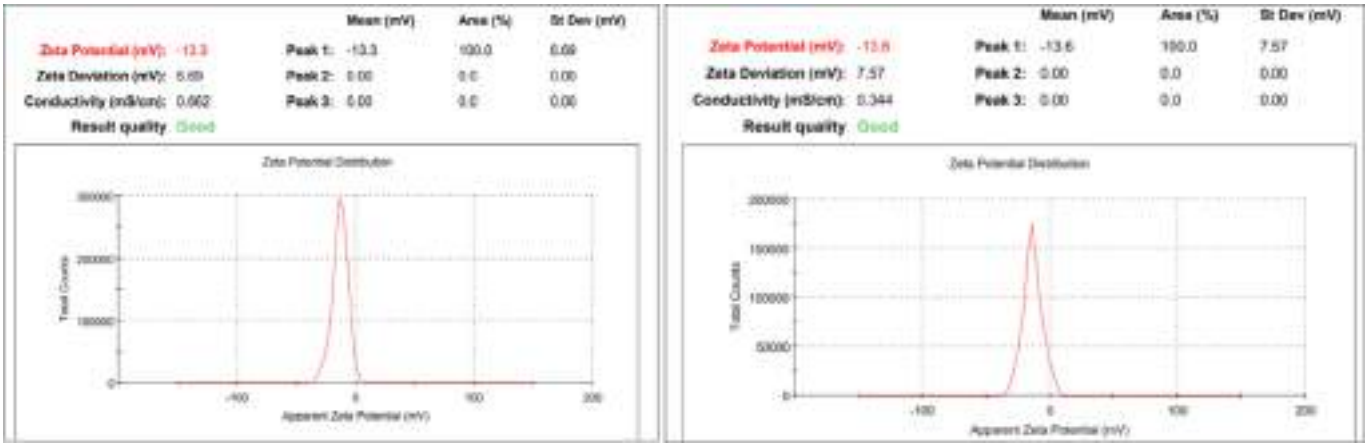

Fig. 1. Zeta potential of a. Blank nanoparticles b. drug-loaded nanoparticles.

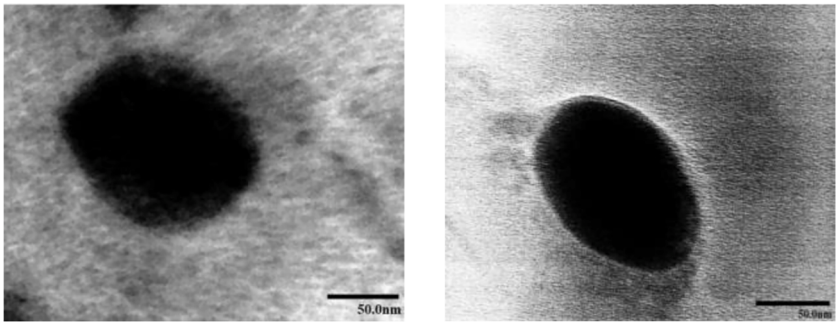

a. **b.**

Fig. 2. HRTEM image of a. blank LION b. drug-loaded nanoparticle (Scale bar = 50 nm).

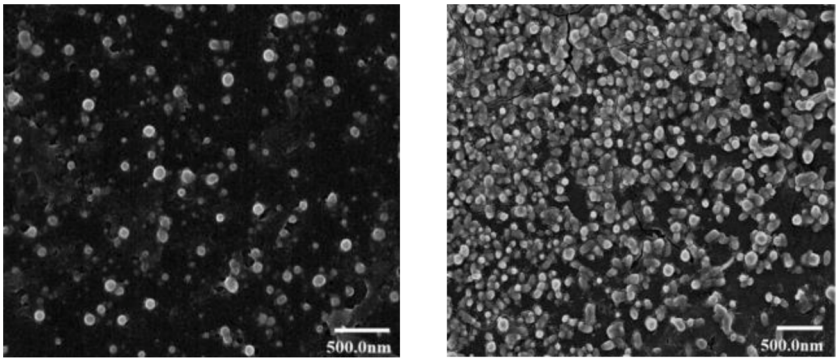

a. **b.**

Fig. 3. FESEM image of a. blank LIONs b. drug-loaded nanoparticles (Scale bar = 500 nm).

The zeta potentials for iron oxide, LIONs, and drug-loaded nanoparticles were recorded to be −11.6, −13.3, and −13.6 mV, respectively (Fig. 1). The preponderance of hydrophobic interactions within the LIONs and drug-loaded nanoparticles translates to increased charge density of the nanoparticles, which, in turn, increases the stability of the dispersions due to higher electrostatic repulsion.

HRTEM micrographs reveal a polyhedral morphology for LIONs as well as drug-loaded nanoparticles, which suggests that incorporation of MTX within the LIONs does not alter their macroscopic structure (Fig. 2). The size histogram is Gaussian and the average diameters of the LIONs and drug-loaded nanoparticles were determined to be 115.03 and 109.36 nm, respectively. These measurements are consistent with the hydrodynamic diameters measured using DLS. Additionally, LIONs exhibited pronounced aggregation compared to the drug-loaded nanoparticles. The magnetism of iron oxide is more pronounced in the former, whereas electrostatic repulsion dominates in the latter system.

Likewise, FESEM micrographs of the LIONs revealed narrowly dispersed, smooth, spherical particle. The average diameter of the particles was estimated to be 114.3 nm. On the other hand, the drug-loaded nanoparticles showed wider distribution with majorly spherical smooth surface for single particles and a few polyhedral with rough surface for agglomerated particles (Fig. 3). Agglomeration of particles could be attributed to the small size and high particle density due to improper dilution or drying during sample preparation. The average size was

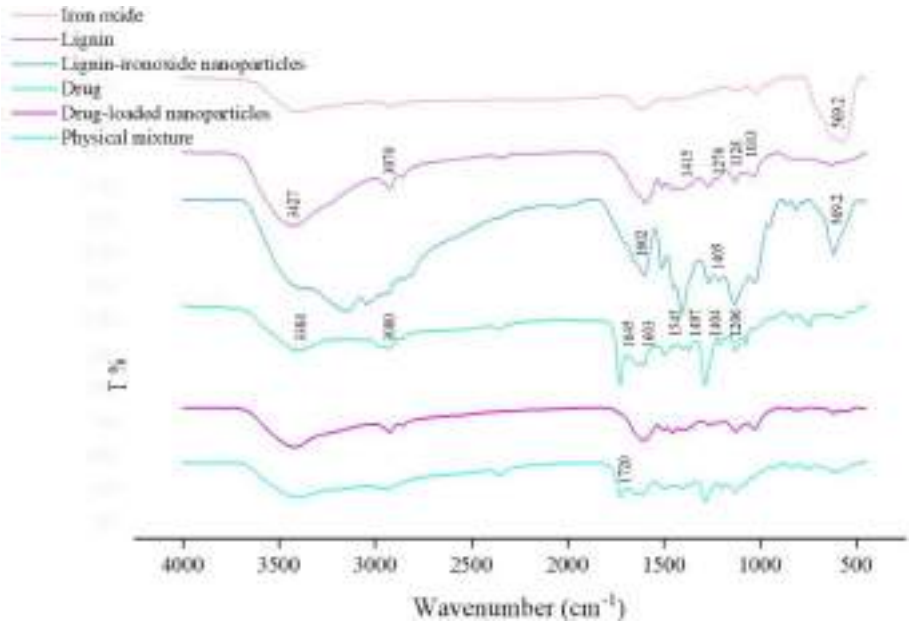

Fig. 4. FT-IR spectra of iron oxide, lignin, LION, drug, drug-loaded nanoparticles, and physical mixture.

129.19 nm which is slightly greater than that observed with DLS and HRTEM data owing to the agglomeration due to the attractive magnetic characteristic of iron oxide [27] and thus, wider size distribution.

3.2.2. FTIR analysis

FT-IR spectra of iron oxide, lignin, LION, drug, drug-loaded nanoparticles, and physical mixture (LION+Drug) (Fig. 4) were recorded to determine the functional groups present and confirm the formation of the nanohybrids by comparing their spectra.

In Fig. 4, the characteristic peak for Fe_3O_4 which is absorption peaks at 570 cm^{-1} belonged to the stretching vibration mode of Fe—O bonds and 3408 cm^{-1} can be attributed to the stretching and bending vibrations of water adsorbed at the surface. In lignin, the bands at 3427 cm^{-1} are due to O—H stretching vibration, and bands near 3070 cm^{-1} are due to asymmetrical C—H stretching vibration. The peaks at 1415 and 1268 cm^{-1} are due to the skeletal vibration and stretching vibration of the aromatic ring, absorption at 1276 cm^{-1} can be attributed to C—O stretch, and 1030–1300 cm^{-1} to C—C, C—O, and ether band. In the spectra of LION, the characteristic peaks of lignin and iron oxide along with more intense peaks at 1405 and 1602 cm^{-1} can be attributed to stretching bands of carboxylate thus, confirming the successful formation of lignin-iron oxide nanoparticles.

For drug (methotrexate hydrate), characteristic absorptions band as a broad signal at 3384 cm^{-1} (O—H stretching from carboxyl groups and water of crystallization), at 3080 cm^{-1} (primary amine N—H stretching), at 1645 and 1603 cm^{-1} is assigned to C═O stretching (from carboxylic and amidic groups). Bands at 1545 and 1497 cm^{-1} correspond to N—H bending from amide overlapping with aromatic –C=C stretching and from 1400 to 1200 cm^{-1} corresponds to –C–O stretching from carboxylic group [28].

The spectra of the drug-loaded nanoparticles and the physical mixture (LION+drug) when compared showed no significant difference except for an extra sharp peak at 1720 cm^{-1} probably due to C═O stretching from carbonyl thus suggesting no drug-polymer interaction and thereby confirming successful drug loading.

3.2.3. DSC

We studied the DSC thermal peaks of the drug and polymer to comprehend their interaction in the formulation. DSC thermal curve of the formulation was compared with pure drug, blank and physical

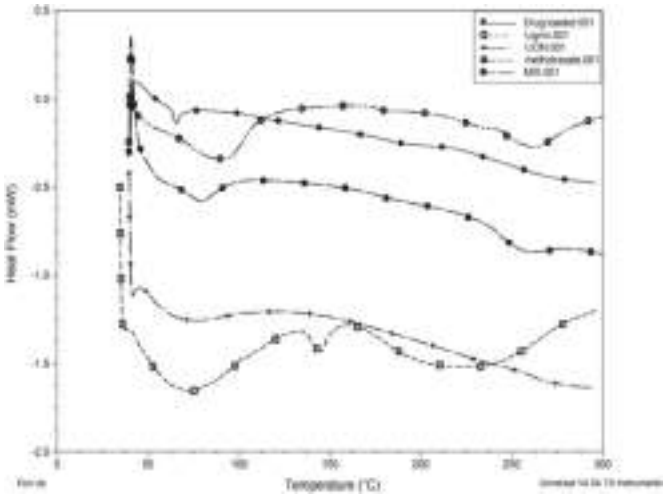

Fig. 5. DSC thermogram of drug-loaded nanoparticles, lignin, LION, drug (methotrexate), and physical mixture (MIX).

Fig. 6. Solution in presence (right) and absence (left) of an external magnetic field a. Blank b. Drug-loaded formulation.

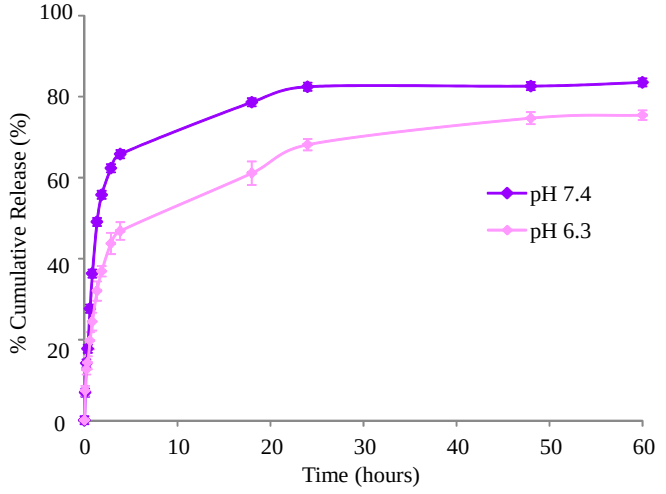

Fig. 7a. Drug release profiles at pH 6.3 and 7.4 (Data represent mean ± SD; $n = 3$).

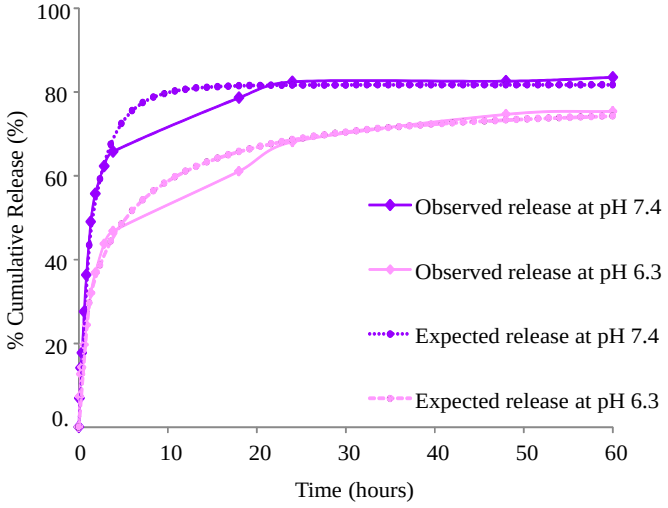

Fig. 7b. Expected & observed drug release profiles at pH 6.3 and 7.4.

mixture (Fig. 5). It was observed that the DSC thermal peak of the physical mixture (LION+drug) was almost similar to that of the pure drug. The endothermic peak corresponding to the dehydration endotherm of MTX slightly shifted to ±3 °C. DSC thermograms demonstrate the absence of characteristic peaks of MTX in formulations confirming encapsulation of drug (MTX) in the nanoparticles.

3.2.4. *pH value and magnetic study*

The pH of a formulation governs its pharmacokinetics, solubility, and even stability. The pH of blank and drug-loaded formulation (1 % *w/v*, 25 °C) was 7.8 ± 0.08 and 7.2 ± 0.12, respectively.

Blank (Fig. 6a) and drug-loaded (Fig. 6b) formulations when placed in an external magnetic field were attracted toward the magnet indicating the retention of the magnetic property of iron oxide. After the removal of the magnetic field, particles were able to redisperse without any residual magnetization. Thus, the loading of the drug retained the magnetic property. Thereby, affirming the potential of the developed formulation as a delivery vehicle for specific targeted delivery in the body that upon exposure to an external magnetic field can be used for hyperthermia in cancer therapy and also serve as a contrast agent in cancer imaging.

3.2.5. *In-vitro drug release studies*

To evaluate the release profile of the formulation, the drug release study was measured at two different pH conditions *i.e.* 7.4 and 6.3. Neutral pH (7.4) as of blood/plasma was chosen to mimic the physiological pH when administered intravenously while pH 6.3 was chosen to mimic the tumor microenvironment.

The drug release followed the same pattern at both pH but with slower release at pH 6.3. % Cumulative release of 83.5 ± 1.2 % and 75.41 ± 1.8 % occurred at 60 h for pH 7.4 and 6.3, respectively with a maximum amount of drug released within 24 h followed by slow sustained release (Fig. 7a). MTX has low solubility in acidic pH and increased solubility was reported when pH was increased from 5 to 7 [29]. The low solubility of MTX at acidic pH may be responsible for the slower release at pH 6.3 [29,30]. This slow release may be exploited to devise a controlled-drug-release system.

3.2.6. *Kinetic modeling*

Kinetic modeling was done to understand the release kinetics of the prepared formulation by applying different equations to the obtained data sets of drug release. Various models were evaluated and the best fit model was selected with R^2 (square of regression coefficient, R) and R^2 adjusted closest to unity *i.e.* Weibull_4 model.

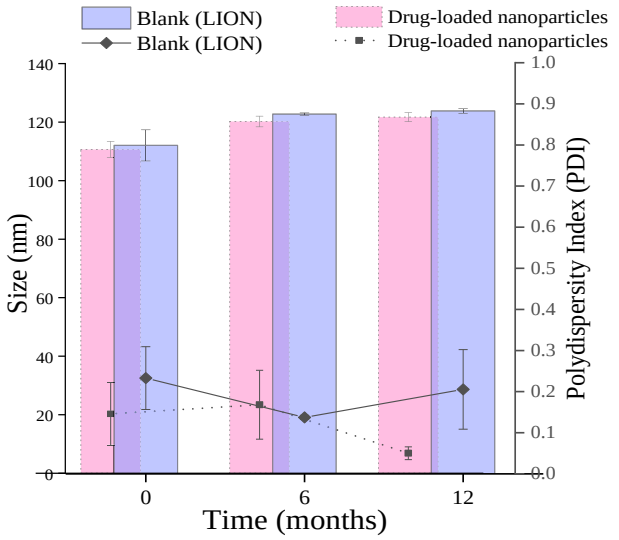

Fig. 8. Stability data of blank and drug-loaded nanoparticles.

The release kinetics followed by Weibull model is given by the equation below:

$$F = F_{max}\left\{1 - e^{-[(t^{*}\beta)/\alpha]}\right\}$$

where F is the fraction of drug dissolved in time t, α is a scale parameter that describes the time scale of the process. The term β is a shape parameter that describes the shape of the curve as either exponential (β = 1), sigmoid (S-shaped) with upward curvature followed by a turning point (β > 1), or parabolic (β < 1), with a higher initial slope and after that consistent with the exponential. The value of β ≤ 0.75 at both pH indicates a release that follows Fickian diffusion through fractal or euclidian spaces [31], thus suggesting fickian release *i.e.* a concentration gradient-dependent release mechanism of the drug through the polymeric matrix. The expected and observed release is shown in Fig. 7b.

3.2.7. *Stability studies*

The stability of a formulation is critically important and therefore, particle size and polydispersity of lyophilized blank and drug-loaded nanoparticles was evaluated for a period of 12 months. The size was observed to be within the desired range with PDI values ≥0.3 in both blank and drug-loaded nanoparticles (Fig. 8). To ensure uniform drug

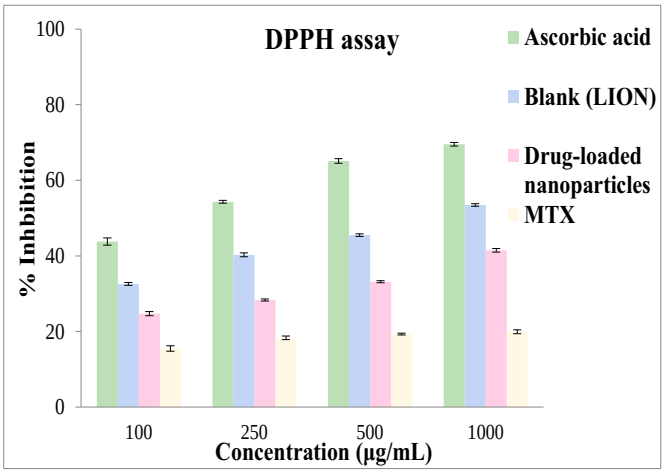

Fig. 9. DPPH assay at different concentrations of ascorbic acid, blank, drug-loaded nanoparticles, and methotrexate. Data represented as mean ± SD; $n = 3$, Statistical analysis was performed using GraphPad Prism, ANOVA test. All values were significant ($p < 0.01$) when compared with standard (ascorbic acid).

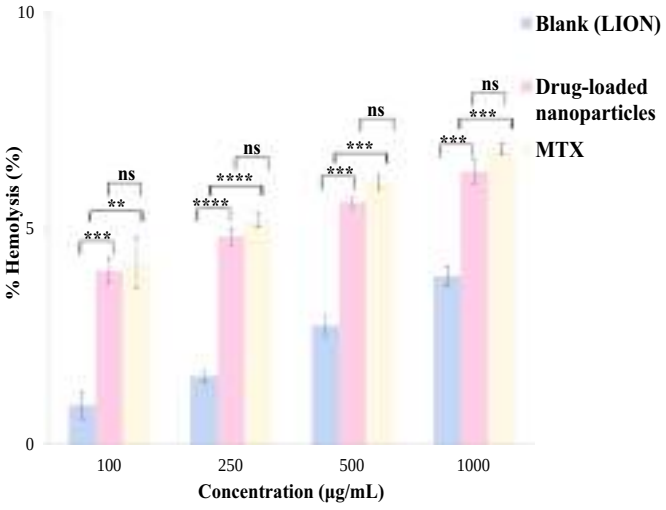

Fig. 10. Hemolytic assay at different concentrations of blank, drug-loaded nanoparticles, and MTX. Data represented as mean ± SD; n = 3, Statistical analysis was performed using GraphPad Prism, ANOVA followed by Tukey's multiple comparison test. Significance was assigned at **p < 0.01, ***p < 0.001, ****p < 0.0001, and ns-non-significant.

content, % drug loading was also measured of drug-loaded nanoparticles. The drug loading was observed to be uniform with 66.06 ± 0.18, 65.89 ± 0.21, and 65.57 ± 0.23 % at 0, 6, and 12 months.

3.2.8. *Antioxidant activity*

The antioxidant property of lignin and iron oxide has been reported before and so, we analyzed that using DPPH assays. A dose-dependent quenching of the DPPH free radicals was observed (Fig. 9) with IC_{50} in the order: ascorbic acid (165.3 ± 13.8 µg/mL) > blank (739.2 ± 43.5 µg/mL) > drug-loaded nanoparticles (921.55 ± 125.45 µg/mL) > methotrexate (46.6 g/mL). Blank and drug-loaded nanoparticles showed good antioxidant property that can be attributed to the polyphenolic groups of lignin and the neutralization of DPPH free-radical by electron transfer by iron oxide [20]. The antioxidant property of the formulation can be used to ameliorate the side effects and organ toxicity caused by methotrexate [32].

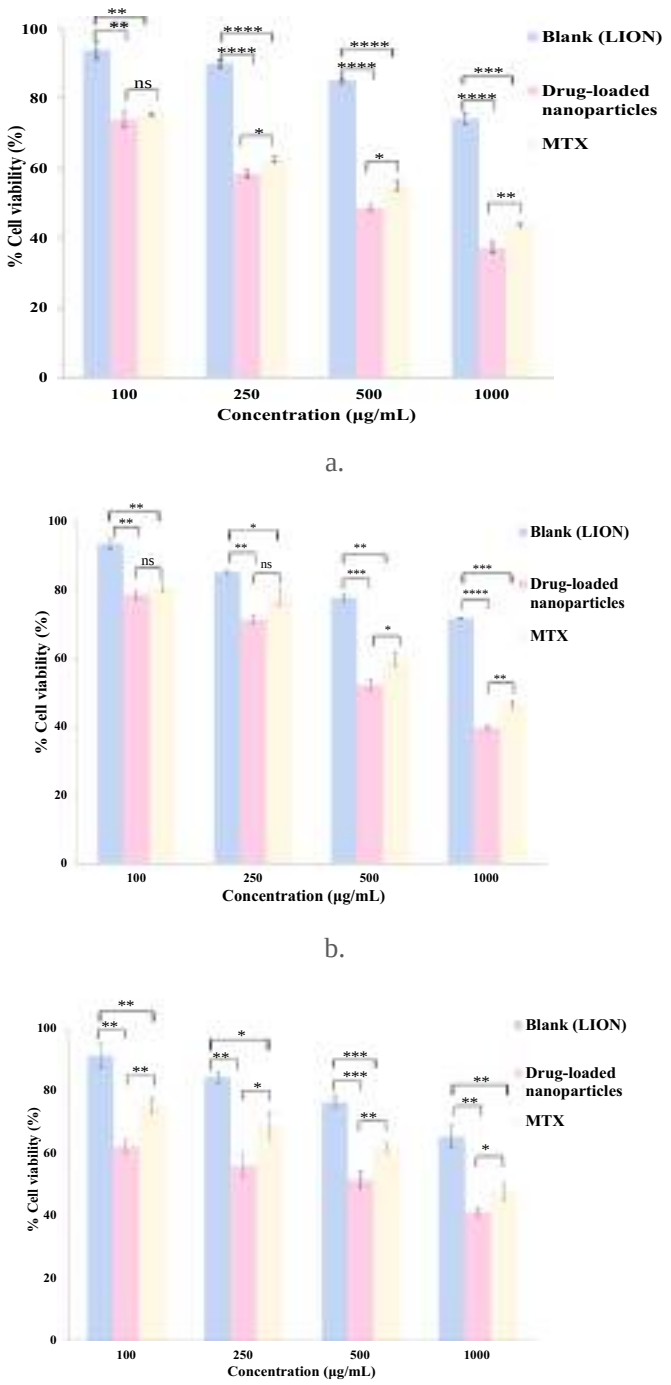

Fig. 11. Cytotoxicity assay at different concentrations of blank, drug-loaded nanoparticles, and MTX against a. RAW cell line b. HeLa cell line c. MDA-MB-231 cell line. Data represented as mean ± SD; $n = 3$, Statistical analysis was performed using GraphPad Prism, ANOVA followed by Tukey's multiple comparison test. Significance was assigned at *p < 0.05, **p < 0.01, ***p < 0.001, ****p < 0.0001, and ns-non-significant.

3.2.9. *Hemotoxicity*

Formulations administered through i.v. route should be compatible with the components of blood and so, hemotoxicity of blank, drug-loaded, and drug was measured at various concentrations (Fig. 10). Any hemolysis value <10 % is considered to be non-hemolytic while a value >25 % hemolysis is considered to be hemolytic [33]. At the highest concentration (1000 µg/mL), the % hemolysis was 3.67 ±

Table 3
IC_{50} values in different cell lines.

IC_{50}(ug/mL)			
Cell line	Blank (LION)	Drug-loaded nanoparticles	MTX
Raw	2789.5 ± 321.5	434.05 ± 81.25	565.2 ± 131.2
HeLa	2113 ± 342	578.6 ± 73.6	789.65 ± 121.45
MDA-MB-231	1711 ± 219	431.9 ± 147.5	733.35 ± 166.55

0.0087, 5.97 ± 0.0096, and 6.3 ± 0.0254 % for blank, drug-loaded, and drug solutions, respectively. These results indicate that the formulation is safe for administration.

3.2.10. Cytotoxicity

The cellular toxicity was evaluated using MTT assay. Different concentrations of LIONs, drug-loaded nanoparticles, and drug alone were evaluated for their cell viability against RAW, HeLa, and MDA-MB-231 cell lines (Fig. 11). All the values were significant ($p < 0.001$) when compared with control. The results showed significant cytotoxicity at the highest concentration (1000 μg/mL) for all the samples. The cytotoxic action of blank nanoparticles at high concentrations could be attributed to the presence of iron oxide. Iron oxide nanoparticles have been reported previously to cause cellular damage and death by causing oxidative stress through increased ROS production (by Fenton reaction, a redox reaction process catalyzed by Fe^{2+}/Fe^{3+}ions) [34], inducing mitochondrial membrane potential collapse and mitochondrial swelling, cytochrome C release [35] and affecting cell homeostasis. Increased ROS

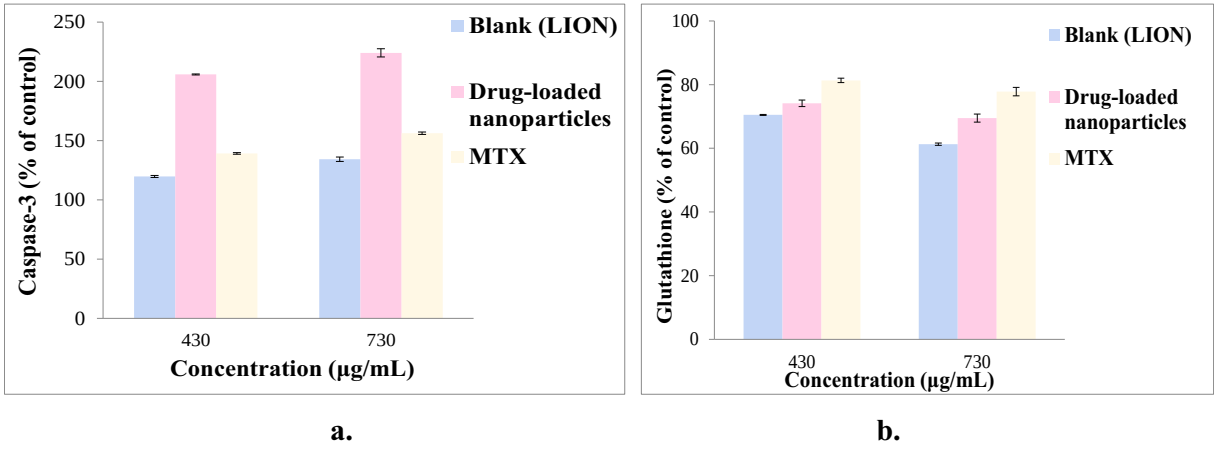

Fig. 12. *In-vitro* assay at different concentrations of blank, drug-loaded nanoparticles, and MTX of a. Caspase-3 and b. Glutathione in breast cancer cells. Data represented as mean ± SD; $n = 3$, Statistical analysis was performed using GraphPad Prism, ANOVA followed by Tukey's multiple comparison test. All values were significant with $p < 0.001$.

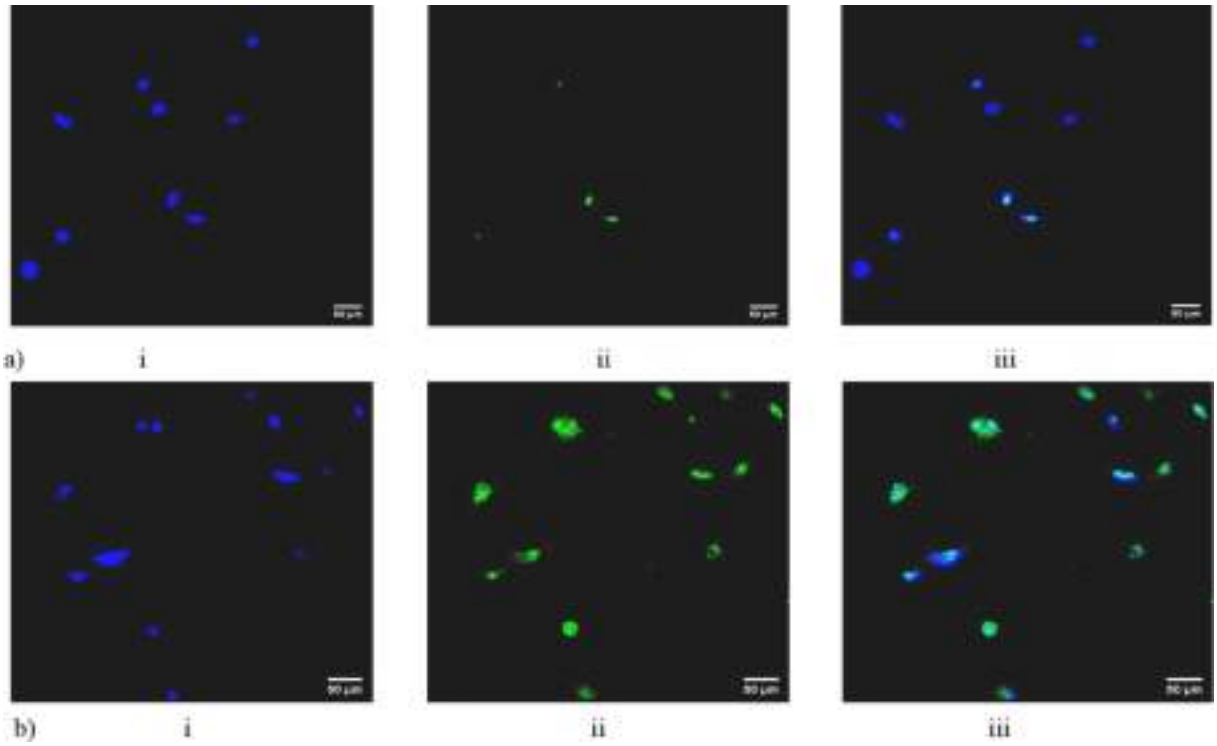

Fig. 13. Confocal microscopy images of MDA-MB-231 cells incubated with a) FITC-labeled-blank and b) FITC-labeled-drug-loaded nanoparticles for 4 h; (i), (ii), and (iii) represent Hoechst fluorescence (blue) FITC fluorescence (green) and merged fluorescence of Hoechst and FITC, respectively. (Scale bar = 50um).

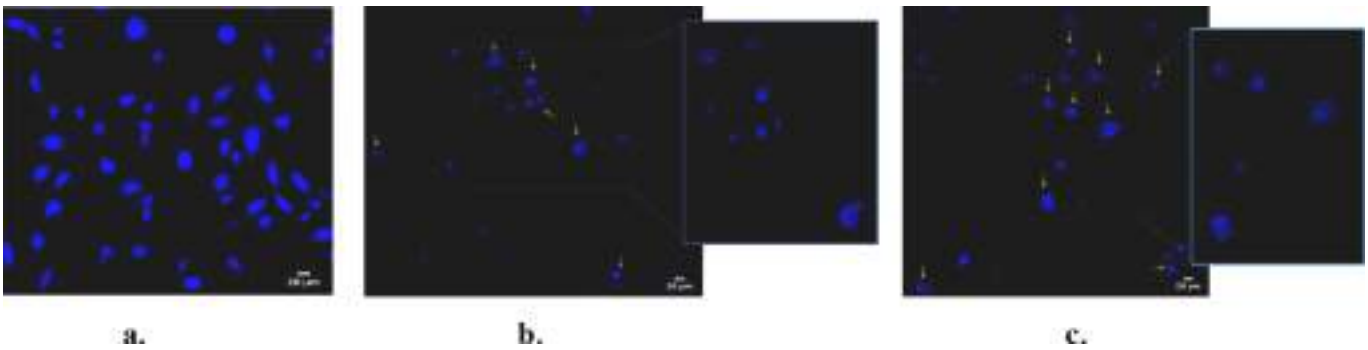

Fig. 14. Confocal microscopy images of MDA-MB-231 cells stained with Hoechst dye a. without treatment (control); after treatment with b. drug-loaded nanoparticles (formulation) and c. MTX (arrow represents DNA fragmentation).

levels result in the disruption of cell wall structure, impaired cellular membrane and nuclear membrane followed by cellular destruction and cell death [36]. The IC_{50} values are given in Table 3. The higher toxicity with formulation than drug alone shows synergistic action of iron-oxide and drug that could be further utilized for dose reduction and, in turn, alleviate the side effects and toxicity related with methotrexate administration.

3.2.11. Caspase-3 and glutathione activity

Caspase-3, an important marker of apoptosis, was induced following treatment with blank, drug-loaded nanoparticles and MTX for 24 h as shown in Fig. 12a. Caspase-3 levels increased in a concentration-dependent manner in all three treatments. Compared to the control group, higher levels were seen after treatment with blank nanoparticles containing iron oxide and lignin, as reported previously [37]. The caspase-3 levels were higher in drug-loaded nanoparticles than MTX alone, suggesting a synergistic action of blank and drug nanoparticles as observed in the cytotoxicity studies.

GSH is one of the most important regulators of intracellular redox balance, performing an antioxidant cell-protective action, cycling between its reduced (GSH) and oxidized forms (GSSG). ROS-mediated apoptotic signaling is associated with a decrease in cellular GSH levels and loss of cellular redox balance and high levels of GSH have been associated with drug resistance [38]. Iron oxide nanoparticles have been previously reported to cause oxidative stress and reduce GSH levels which are influenced by the size and oxidation state of iron [38]. Iron oxide nanoparticle-induced oxidative stress was evident by drastic depletion of GSH levels on treatment with blank nanoparticles. As shown in Fig. 12b, the reduction in drug-loaded nanoparticles was higher than with MTX. It has been demonstrated that GSH plays a possible role in MTX-induced apoptosis by contributing to maintaining cytochrome *c* in its reduced state under physiological conditions and preventing its apoptotic effect. Therefore, GSH depletion would favor cytochrome *c*-induced apoptosis by MTX [38]. The reduction in GSH levels by iron oxide nanoparticles could potentiate the action of MTX by inducing apoptosis mediated by cytochrome *c* release asserting the synergistic cytotoxicity of drug-loaded nanoparticles.

3.2.12. Cellular uptake

We analyzed the cellular uptake of FITC-labeled nanoparticles using confocal fluorescence imaging. For imaging, nuclei of cells were stained with Hoechst 33342 (blue). The fluorescence images confirmed the internalization of FITC-labeled nanoparticles within 4 h in breast carcinoma cell line (Fig. 13). Importantly, it can be seen that the fluorescence intensity of drug-loaded nanoparticles was stronger than blank nanoparticles which can be attributed to the greater receptors-mediated endocytosis of methotrexate loaded nanoparticles. Thus, it indicates that the developed blank system could be used as a vehicle for drug delivery, especially for poorly water-soluble drugs like methotrexate.

3.2.13. Nuclear condensation and DNA fragmentation

The MDA-MB-231 cells were treated with 1 mg/mL doses of drug-loaded nanoparticles and MTX for 24 h. Cells were stained with Hoechst 33342 DNA that binds to adenine-thymine-rich regions of DNA and stain the minor groove. The shape of untreated cells showed normal morphology with majorly spindle and some round-shaped cells and formed a complete sheet with 60–70 % confluency (Fig. 14a). The cells incubated with drug-loaded nanoparticles and MTX (Fig. 14b and c) showed decreased growth and apoptotic features like cellular rounding, and shrinkage, along with nuclear condensation and DNA fragmentation, indicated by an arrow. The observed cellular damage was slightly higher in drug-loaded nanoparticles than in the drug alone, thus supporting the synergistic action of iron oxide, lignin, and methotrexate, as observed in cytotoxicity studies.

4. Conclusion

We have developed a nano-based biopolymeric magnetic delivery system for chemotherapy. The magnetic nanoparticles were prepared using the newer approach of combining two different methods of nanoparticle preparation *i.e.*, anti-solvent precipitation and ultrasonication. The nanoparticles prepared with the new approach were better based on their size, range and uniformity. The nanoparticles were further optimized by varying the lignin-to-drug ratio and evaluated for physicochemical characteristics. Our synthetic scheme achieves a lignin-to-drug ratio of 1:3, and drug loading and encapsulation efficiencies of 66.06 % and 64.88 %, respectively. The pH of the formulation was near neutral. Moreover, the nanoparticles retain their magnetism and bear a polyhedral geometry. The particles also have a characteristic dimension of 110–130 nm, which makes them well-suited for rapid uptake into cancer cells on account of receptor-mediated endocytosis. We confirmed these conclusions in breast cancer and macrophage cellular assays. In fsact, the nanoparticles are non-hemolytic and markedly more cytotoxic compared to the pure drug and they also exhibit a concentration-dependent release of MTX for the initial 24 h, followed by slow, sustained release. The higher cytotoxicity of the nanoparticles confirms the lignin, iron oxide, and, to an extent MTX act synergistically to enhance caspase-3 activity and reduce glutathione levels in the breast cancer cells. Additionally, the radical scavenging activity of nanoparticles can be attributed to lignin's high anti-oxidant effect. These results confirm that not only does our novel design overcome MTX's limitations, but the system's physicochemical properties, release kinetics, and biological activity make it a highly effective anti-cancer treatment. Our work advocates the inordinate potential of nano-based magnetic biopolymeric systems in drug delivery and cancer therapy. These conclusions, in conjunction with the fact that lignin is an excellent chassis for chemical modification, and will pave the way for the development of 'intelligent' lignin-based theranostic nanoprobes that could significantly be more efficacious than current therapeutics.

Credit authorship contribution statement

Khushboo Pathania: Investigation, Writing- Original draft preparation, Methodology, Validation**. Sangeeta P. Sah:**: Supervision, Writing - Review & Editing. **Deepak Salunke:** Resources, Writing - Review & Editing. **Manish Jain:** Formal analysis, Data collection. **Ashok Kumar Yadav:** Resources, Data collection**, Vikramaditya G. Yadav:** Conceptualization, Writing - Review & Editing**. Sandip V. Pawar:** Conceptualization, Supervision, Project administration, Writing- Original draft preparation, Writing - Review & Editing, Funding acquisition.

Declaration of competing interest

The authors declare that they have no known competing financial interests or personal relationships that could have appeared to influence the work reported in this paper.

Data availability

Data will be made available on request.

Acknowledgment

SVP gratefully acknowledge financial support from Department of Science & Technology & Renewable Energy, Chandigarh Administration. Chandigarh (UT), India (Grant no: S&T&RE/RP/147/FY(21-22)/AN10/2021/1013-1020) and from University Grants Commission, New Delhi for UGC- Start up grant No. F.4-5(65-FRP) (lv-cycle)/2017(BSR) under UGC Faculty Recharge Programme (UGC-FRP). KP is grateful to Council of Scientific & Industrial Research (CSIR) for her Junior Research Fellowship (JRF) [File No: 09/0135(13255)/2022-EMRI].

References

[1] H. Sung, J. Ferlay, R.L. Siegel, M. Laversanne, I. Soerjomataram, A. Jemal, F. Bray, Global Cancer Statistics 2020: GLOBOCAN estimates of incidence and mortality worldwide for 36 cancers in 185 countries, CA Cancer J. Clin. 71 (2021) 209–249, https://doi.org/10.3322/caac.21660.

[2] S. Senapati, A.K. Mahanta, S. Kumar, P. Maiti, Controlled drug delivery vehicles for cancer treatment and their performance, Signal Transduct. Target. Ther. 3 (2018) 7, https://doi.org/10.1038/s41392-017-0004-3.

[3] D. Chenthamara, S. Subramaniam, S.G. Ramakrishnan, S. Krishnaswamy, M. M. Essa, F.-H. Lin, M.W. Qoronfleh, Therapeutic efficacy of nanoparticles and routes of administration, Biomater. Res. 23 (2019) 20, https://doi.org/10.1186/s40824-019-0166-x.

[4] J. Fang, H. Nakamura, H. Maeda, The EPR effect: unique features of tumor blood vessels for drug delivery, factors involved, and limitations and augmentation of the effect, Adv. Drug Deliv. Rev. 63 (2011) 136–151, https://doi.org/10.1016/j.addr.2010.04.009.

[5] Y. Shi, R. van der Meel, X. Chen, T. Lammers, The EPR effect and beyond: strategies to improve tumor targeting and cancer nanomedicine treatment efficacy, Theranostics 10 (17) (2020) 7921–7924, https://doi.org/10.7150/thno.49577.

[6] D. Peer, J.M. Karp, S. Hong, O.C. Farokhzad, R. Margalit, R. Langer, Nanocarriers as an emerging platform for cancer therapy, Nat. Nanotechnol. 2 (2007) 751–760, https://doi.org/10.1038/nnano.2007.387.

[7] Q.Y. Wei, Y.M. Xu, A.T.Y. Lau, Recent progress of nanocarrier-based therapy for solid malignancies, Cancers 12 (2020) 1–37, https://doi.org/10.3390/cancers12102783 (Basel).

[8] C.N. Dong, J.A. Tate, W.C. Kett, J. Batra, E. Demidenko, L.D. Lewis, P.J. Hoopes, T. U. Gerngross, K.E. Griswold, Tumor cell targeting by iron oxide nanoparticles is dominated by different factors in vitro versus in vivo, PLoS One 10 (2015) 1–18, https://doi.org/10.1371/journal.pone.0115636.

[9] R. Vakili-Ghartavol, A.A. Momtazi-Borojeni, Z. Vakili-Ghartavol, H.T. Aiyelabegan, M.R. Jaafari, S.M. Rezayat, S. Arbabi Bidgoli, Toxicity assessment of superparamagnetic iron oxide nanoparticles in different tissues, Artif. Cells Nanomed. Biotechnol. 48 (2020) 443–451, https://doi.org/10.1080/21691401.2019.1709855.

[10] M. Osaci, M. Cacciola, Influence of the magnetic nanoparticle coating on the magnetic relaxation time, Beilstein J. Nanotechnol. 11 (2020) 1207–1216, https://doi.org/10.3762/bjnano.11.105.

[11] L. Chen, Y. Shi, B. Gao, Y. Zhao, Y. Jiang, Z. Zha, W. Xue, L. Gong, Lignin nanoparticles: green synthesis in a γ-valerolactone/water binary solvent and application to enhance antimicrobial activity of essential oils, ACS Sustain. Chem. Eng. 8 (2020) 714–722, https://doi.org/10.1021/acssuschemeng.9b06716.

[12] M. Culebras, M. Pishnamazi, G.M. Walker, M.N. Collins, Facile tailoring of structures for controlled release of paracetamol from sustainable lignin derived platforms, Molecules 26 (2021) 1–9, https://doi.org/10.3390/molecules26061593.

[13] V.K. Thakur, M.K. Thakur, Recent advances in green hydrogels from lignin: a review, Int. J. Biol. Macromol. 72 (2015) 834–847, https://doi.org/10.1016/j.ijbiomac.2014.09.044.

[14] P. Jędrzejczak, M.N. Collins, T. Jesionowski, Ł. Klapiszewski, The role of lignin and lignin-based materials in sustainable construction – a comprehensive review, Int. J. Biol. Macromol. 187 (2021) 624–650, https://doi.org/10.1016/j.ijbiomac.2021.07.125.

[15] A. Beaucamp, M. Muddasar, T. Crawford, M.N. Collins, M. Culebras, Sustainable lignin precursors for tailored porous carbon-based supercapacitor electrodes, Int. J. Biol. Macromol. 221 (2022) 1142–1149, https://doi.org/10.1016/j.ijbiomac.2022.09.097.

[16] B.R. Giri, J.S. Kim, J.H. Park, S.G. Jin, K.S. Kim, F. Ud Din, H.G. Choi, D.W. Kim, Improved bioavailability and high photostability of methotrexate by spray-dried surface-attached solid dispersion with an aqueous medium, Pharmaceutics 13 (2021) 1–14, https://doi.org/10.3390/pharmaceutics13010111.

[17] Y.zhi Ma, D.feng Zheng, Z.ye Mo, R.jing Dong, X.qing Qiu, Magnetic lignin-based carbon nanoparticles and the adsorption for removal of methyl orange, Colloids Surf. A Physicochem. Eng. Asp. 559 (2018) 226–234, https://doi.org/10.1016/j.colsurfa.2018.09.054.

[18] L. Dai, R. Liu, L.Q. Hu, Z.F. Zou, C.L. Si, Lignin nanoparticle as a novel green carrier for the efficient delivery of resveratrol, ACS Sustain. Chem. Eng. 5 (2017) 8241–8249, https://doi.org/10.1021/acssuschemeng.7b01903.

[19] Z. Liu, L. Yang, Antisolvent precipitation for the preparation of high polymeric procyanidin nanoparticles under ultrasonication and evaluation of their antioxidant activity in vitro, Ultrason. Sonochem. 43 (2018) 208–218, https://doi.org/10.1016/j.ultsonch.2018.01.019.

[20] J. Sandhya, S. Kalaiselvam, Biogenic synthesis of magnetic iron oxide nanoparticles using inedible Borassus flabellifer seed coat: characterization, antimicrobial, antioxidant activity and in vitro cytotoxicity analysis, Mater. Res. Express 7 (2020) 15045, https://doi.org/10.1088/2053-1591/ab6642.

[21] J.O. Muga, J.W. Gathirwa, M. Tukulula, W.G.Z.O. Jura, In vitro evaluation of chloroquine-loaded and heparin surface-functionalized solid lipid nanoparticles, Malar. J. 17 (2018) 1–7, https://doi.org/10.1186/s12936-018-2302-9.

[22] E. Ahmadian, A. Eftekhari, T. Kavetskyy, A.Y. Khosroushahi, V.A. Turksoy, R. Khalilov, Effects of quercetin loaded nanostructured lipid carriers on the paraquat-induced toxicity in human lymphocytes, Pestic. Biochem. Physiol. 167 (2020), 104586, https://doi.org/10.1016/j.pestbp.2020.104586.

[23] A. Hasanzadeh, B. Gholipour, S. Rostamnia, A. Eftekhari, A. Tanomand, K. A. Valizadeh, S. Khaksar, R. Khalilov, Biosynthesis of AgNPs onto the urea-based periodic mesoporous organosilica (AgxNPs/Ur-PMO) for antibacterial and cell viability assay, J. Colloid Interface Sci. 585 (2021) 676–683, https://doi.org/10.1016/j.jcis.2020.10.047.

[24] M.S. Alqahtani, A. Alqahtani, A. Al-Thabit, M. Roni, R. Syed, Novel lignin nanoparticles for oral drug delivery, J. Mater. Chem. B 7 (2019) 4461–4473, https://doi.org/10.1039/c9tb00594c.

[25] H. Moghtaderi, H. Sepehri, L. Delphi, F. Attari, Gallic acid and curcumin induce cytotoxicity and apoptosis in human breast cancer cell MDA-MB-231, BioImpacts 8 (2018) 185–194, https://doi.org/10.15171/bi.2018.21.

[26] C.-W. Wu, H.-C. Liu, Y.-L. Yu, Y.-T. Hung, C.-W. Wei, G.-T. Yiang, Combined treatment with vitamin C and methotrexate inhibits triple-negative breast cancer cell growth by increasing H2O2 accumulation and activating caspase-3 and p38 pathways, Oncol. Rep. 37 (2017) 2177–2184, https://doi.org/10.3892/or.2017.5439.

[27] Ł. Klapiszewski, J. Zdarta, K. Antecka, K. Synoradzki, K. Siwińska-Stefańska, D. Moszyński, T. Jesionowski, Magnetite nanoparticles conjugated with lignin: a physicochemical and magnetic study, Appl. Surf. Sci. 422 (2017) 94–103, https://doi.org/10.1016/j.apsusc.2017.05.255.

[28] A. Fuliaș, C. Popoiu, G. Vlase, T. Vlase, D. Oneţiu, G. Săvoiu, G. Simu, C. Pătruţescu, G. Ilia, I. Ledeți, Thermoanalytical and spectroscopic study on methotrexate - active substance and tablet, Dig. J. Nanomater. Biostruct. 9 (2014) 93–98.

[29] C.N. Cheaburu Yilmaz, D. Pamfil, C. Vasile, N. Bibire, R.V. Lupuşoru, C.L. Zamfir, C.E. Lupusoru, Toxicity, biocompatibility, pH-responsiveness and methotrexate release from pva/hyaluronic acid cryogels for psoriasis therapy, Polymers 9 (2017) 1–19, https://doi.org/10.3390/polym9040123 (Basel).

[30] F. Ullah, Z. Iqbal, A. Khan, S.A. Khan, L. Ahmad, A. Alotaibi, R. Ullah, M. Shafique, Formulation development and characterization of pH responsive polymeric nano-pharmaceuticals for targeted delivery of anti-cancer drug (methotrexate), Front. Pharmacol. 13 (2022) 1–13, https://doi.org/10.3389/fphar.2022.911771.

[31] V. Papadopoulou, K. Kosmidis, M. Vlachou, P. Macheras, On the use of the Weibull function for the discernment of drug release mechanisms, Int. J. Pharm. 309 (2006) 44–50, https://doi.org/10.1016/j.ijpharm.2005.10.044.

[32] N. Vardi, H. Parlakpinar, A. Cetin, A. Erdogan, I. Cetin Ozturk, Protective effect of β-carotene on methotrexate-induced oxidative liver damage, Toxicol. Pathol. 38 (2010) 592–597, https://doi.org/10.1177/0192623310367806.

[33] K. Amin, R. Dannenfelser, Vitro Hemolysis: Guidance for the Pharmaceutical Scientist, J. Pharm. Sci. 95 (2006) 1173–1176, https://doi.org/10.1002/jps.20627.

[34] E. Laqué-Rupérez, M.J. Ruiz-Gómez, L. De La Peña, L. Gil, M. Martínez-Morillo, Methotrexate cytotoxicity on MCF-7 breast cancer cells is not altered by exposure to 25 Hz, 1.5 mT magnetic field and iron (III) chloride hexahydrate, Bioelectrochemistry 60 (2003) 81–86, https://doi.org/10.1016/S1567-5394(03)00054-9.

[35] J. Jahanbani, M. Ghotbi, F. Shahsavari, E. Seydi, S. Rahimi, J. Pourahmad, Selective anticancer activity of superparamagnetic iron oxide nanoparticles (SPIONs) against oral tongue cancer using in vitro methods: the key role of oxidative stress on cancerous mitochondria, J. Biochem. Mol. Toxicol. 34 (2020) 1–8, https://doi.org/10.1002/jbt.22557.

[36] A. Baran, M.F. Baran, C. Keskin, S.I. Kandemir, M. Valiyeva, S. Mehraliyeva, R. Khalilov, A. Eftekhari, Ecofriendly/rapid synthesis of silver nanoparticles using extract of waste parts of artichoke (Cynara scolymus L.) and evaluation of their cytotoxic and antibacterial activities, J. Nanomater. 2021 (2021), https://doi.org/10.1155/2021/2270472.

[37] S. Barros, N. Mencia, L. Rodríguez, C. Oleaga, C. Santos, V. Noé, C.J. Ciudad, The redox state of cytochrome C modulates resistance to methotrexate in human MCF7 breast cancer cells, PLoS One 8 (2013), e63276, https://doi.org/10.1371/journal.pone.0063276.

[38] Z. Yarjanli, K. Ghaedi, A. Esmaeili, S. Rahgozar, A. Zarrabi, Iron oxide nanoparticles may damage to the neural tissue through iron accumulation, oxidative stress, and protein aggregation, BMC Neurosci. 18 (2017) 1–12, https://doi.org/10.1186/s12868-017-0369-9.

Materials Letters 337 (2023) 133956

Contents lists available at ScienceDirect

Materials Letters

journal homepage: www.elsevier.com/locate/matlet

Lignin-chitosan biocomposite film for antimicrobial activity: Fabrication, characterization and *in-vitro* evaluation

Pritiman Pothal [a,1], Khushboo Pathania [a,1], Sunil Kumar [a], Jasdeep Kaur [b], Sangeeta P. Sah [a], Rachna Singh [b], Sandip V. Pawar [a,*]

[a] University Institute of Pharmaceutical Sciences, Panjab University, Chandigarh 160014, India
[b] Department of Microbial Biotechnology, Panjab University, Chandigarh 160014, India

ARTICLE INFO

Keywords:
Biomaterials
Lignin
Chitosan
Polymers
Thin films
Wound healing

ABSTRACT

Lignin and chitosan are natural polymers that exhibit antioxidant and wound-healing properties, respectively. In this study, lignin-chitosan polymeric films were prepared using solvent-casting method. Physicochemical characterization of prepared films was carried out using FESEM, FTIR and DSC. An antibiotic neomycin sulphate was loaded onto films and drug-release profile, antioxidant activity, hemolytic activity, cell viability and antimicrobial activity of film were evaluated. The films were observed to be smooth and have uniform surface with homogenous and fibrous nature. The cumulative release of 97.94% in 8 h was observed in drug release study and it followed Weibull_4 order release kinetics. The film was non-hemolytic and exhibited excellent antioxidant activity with no toxicity towards fibroblast cells. Additionally, the drug-loaded film showed significant antimicrobial activity against both Gram-negative and Gram-positive bacteria.

1. Introduction

Biopolymers are natural polymers with immense potential and have recently gained great importance in protection of damaged skin from infections and dehydration. We employed two biopolymers, lignin, and chitosan for facile preparation of polymeric film. The polymeric film can serve as a drug delivery cargo with great potential in topical applications especially in skin infection and wound treatment. In this study, an antibiotic neomycin sulphate was entrapped in polymeric film and drug-loaded film was tested for antimicrobial activity for its possible application in skin protection during wound/injury. Lignin is the second most abundant natural polymer with antioxidant, antimicrobial, UV-absorption property and abundant functional groups rendering it susceptible for chemical modification [1]. Chitosan is a heteropolysaccharide formed by deacetylation of chitin, an abundant biopolymer extracted from insects/crustacean shells/mushroom cell-wall. It possesses bio-adhesive, antimicrobial, anti-inflammatory, wound healing, and film-forming characteristics [2]. Neomycin sulphate is an aminoglycoside antibiotic that acts by inhibiting bacterial protein synthesis [3]. The films were prepared using solvent-casting method and dried by four different methods. The effects of drug loadings on film characteristics were carried out based on several properties, such as surface morphology, structural changes, and thermal behaviour. *In-vitro* drug release study followed by *in-vitro* evaluation for hemocompatibility and cellular toxicity was carried out. Additionally, antioxidant and antibacterial activity of prepared films were also evaluated using free radical scavenging and zone of growth inhibition assay.

2. Materials and methods

Alkali lignin was purchased from Sigma-Aldrich, chitosan was purchased from Central Drug House (P) Ltd., neomycin sulphate, and 2,2-diphenyl-1-picrylhydrazyl (DPPH) were purchased from HiMedia Laboratories Pvt. Ltd. Films were prepared using solvent-casting method as reported before with minor modifications [4]. Lignin solution (10 % w/v in water) and chitosan solution (10 % w/v in 3 % glacial acetic acid) was stirred at 350 rpm for 24 h. Lignin solution was added dropwise to chitosan solution under stirring and it was maintained for 24 h. The solutions were mixed to obtain three different ratios of lignin:chitosan (1:1, 1:5, and 1:10). The final solution was dried by four different methods (Fig. 1). The prepared lignin-chitosan solutions were dried at room temperature (25 °C) for 4–5 days (air-drying) or using a hot air

* Corresponding author.
E-mail address: pawars@pu.ac.in (S.V. Pawar).
[1] Authors contributed equally.

https://doi.org/10.1016/j.matlet.2023.133956
Received 25 October 2022; Received in revised form 16 January 2023; Accepted 23 January 2023
Available online 25 January 2023

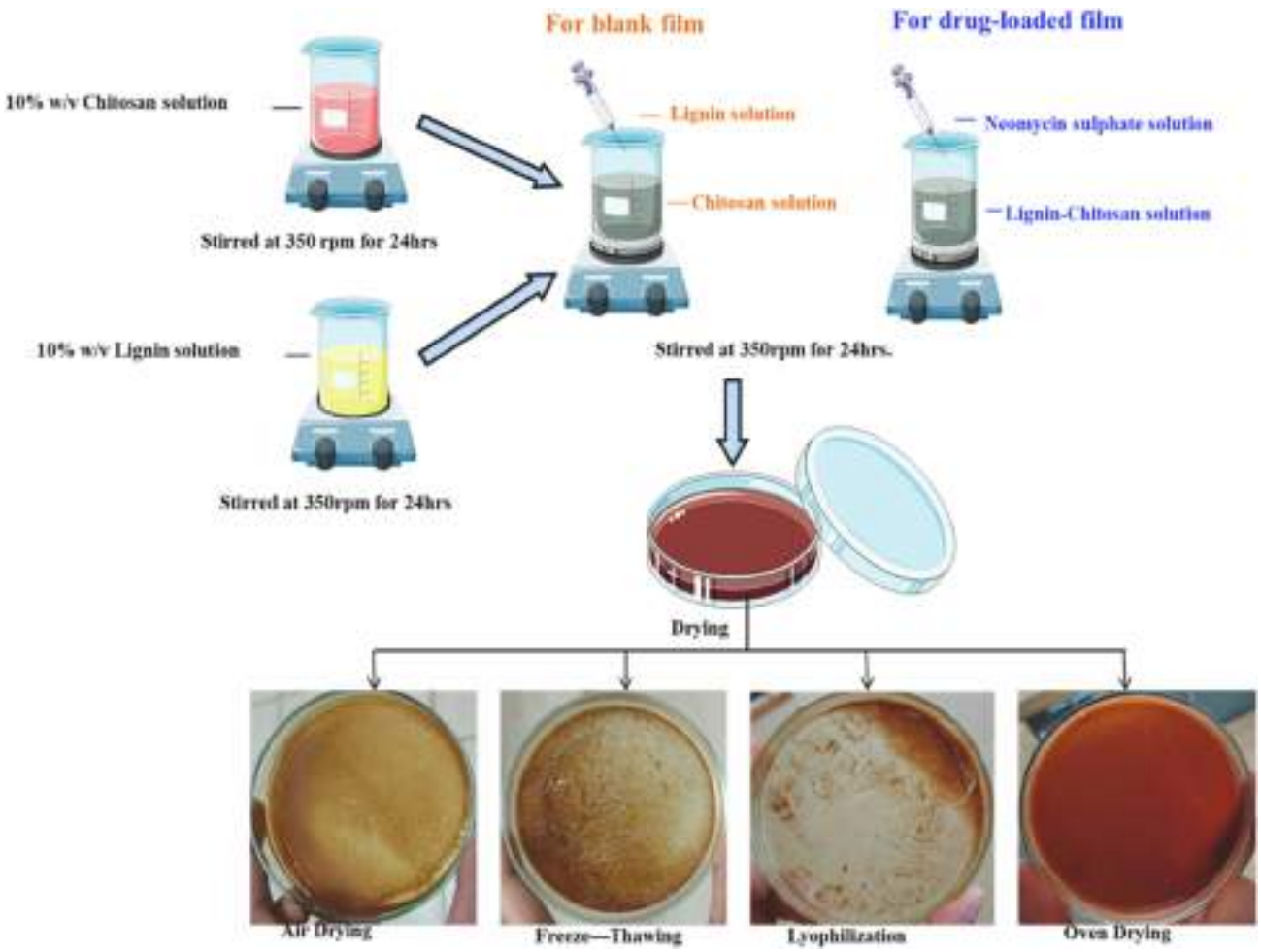

Fig. 1. Schematic of preparation of blank and drug-loaded film.

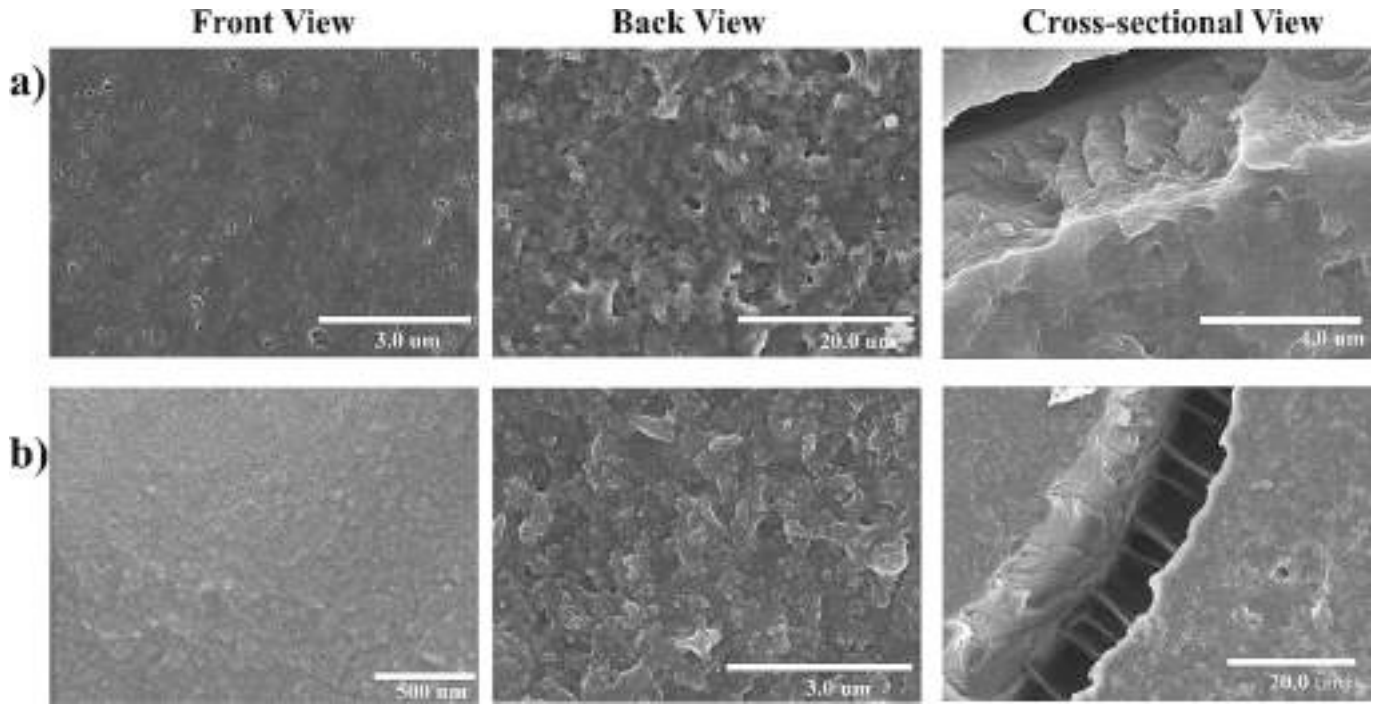

Fig. 2. FESEM images of a) Blank film b) Drug-loaded film.

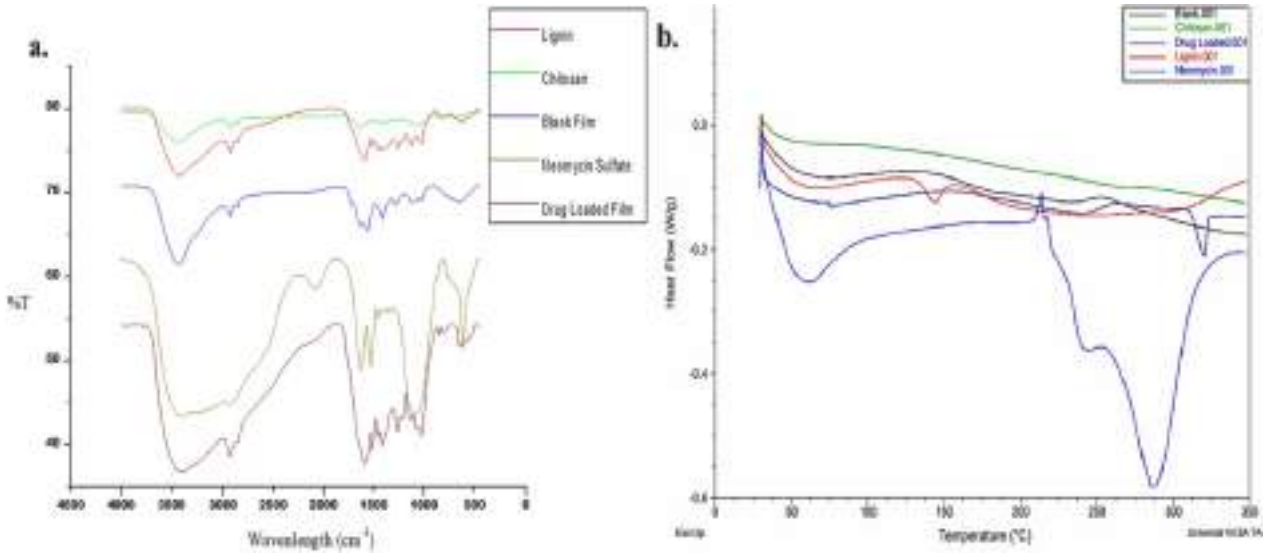

Fig. 3. a. FTIR spectra b. DSC thermogram.

oven at 50 °C for 18–20 h (oven-drying), or with multiple freeze-thawing cycles by freezing for six-hour followed by 12 h thawing (freeze-thawing) or lyophilized. For drug loading, in-situ addition method was employed. Neomycin sulphate (5, 10 & 15 mg/ml) was added dropwise to the lignin-chitosan solution under stirring and stirring was maintained for 24 h (Fig. 1).

3. Characterization of film

The film was characterized using Field Emission Scanning Electron Microscopy (FESEM) (SU8010 series, Hitachi, Japan), Fourier-transform Infrared (FTIR) (Perkin Elmer FT-IR spectrometer) and Differential Scanning Calorimetry (DSC) (DSC 6Q20-TA, Waters, USA) instrument with heating rate of 10 °C/min from 30 °C to 350 °C. *In-vitro* drug release experiments were carried out at pH 7.4 and was analyzed using UV–visible spectrophotometer (UV 3200, Labindia Analytical) at 350 nm. Rat blood was used to determine ex-vivo hemolytic activity where 1 % v/v Triton X-100 and phosphate buffer saline used as positive and negative control, respectively [5]. DPPH assay was used to assess the antioxidant potential [4]. McCoy fibroblast cells were used to investigate the cytotoxicity of film through 3-(4,5-dimethylthiazol-2-yl)-2,5-diphenyltetrazolium bromide (MTT) assay [6]. The antimicrobial activity was determined against *Escherichia coli* ATCC (American Type Culture Collection) 25,922 and *Staphylococcus aureus* ATCC 29213 by following the method of disk-diffusion assay according to the guidelines of Clinical and Laboratory Standards Institute (CLSI) [7]. Blank films, drug-only controls, and positive control [*E. coli*, ciprofloxacin (5 μg); *S. aureus*, amikacin (30 μg)] were set up in parallel. The plates were incubated at 37 °C for 18 h and the diameters of the growth-inhibition zones were measured up to the nearest whole millimetres. All experiments were performed in triplicate and repeated twice to confirm the observations.

4. Results and discussion

4.1. Optimization studies

Solvent-casting method was used with varying ratios of lignin-chitosan mixture and four different drying techniques (Fig. 1). From all the tried ratios and methods, the 1:5 lignin:chitosan ratio and oven drying method yielded uniform homogenous film with a smooth front and slightly rough back surface. All other methods resulted in uneven drying and non-uniform films. Therefore, films obtained by oven-drying method were selected for further evaluation.

4.2. Characterization of films

Surface of the film was homogenous & fibrous with a polymeric network where drug was encapsulated (Fig. 2). The drug loading improved the fibrous nature of the film as evident by the micrographs (Fig. 2) possibly by hydrogen bonding and infusing in the intermolecular spaces. The fibrous nature aids in wound healing by increasing oxygen supply to the wound and providing attachment to the epidermis layer [8].

The FTIR spectra (Fig. 3a) for lignin showed characteristic peak at 3419.40 cm^{-1} (O—H stretching vibration), near 2857.30 cm^{-1} (asymmetrical C—H stretching vibration), at 1592 and 1518.70 cm^{-1} (skeletal vibration and stretching vibration of the aromatic ring), at 1274.6 cm^{-1} (C—O stretch), and 1030–1300 cm^{-1} (C—C, C—O and ether band). In chitosan, the characteristic peak were observed at 3366.13 cm^{-1} (N—H stretching), 2925.96 cm^{-1} (–CH2-asymmetric stretching), 2855.2 cm^{-1} (–CH2-symmetric stretching), 1555.5 cm^{-1} (C═O stretching), 1413.79 cm^{-1} (N—H bending), 1158.50 cm^{-1} (asymmetric C—O—C stretching vibrations). Blank film showed the characteristic peaks of both lignin and chitosan and similarly drug-loaded film showed the characteristic peaks of neomycin, lignin, and chitosan, with broader peaks than blank film at 3400 cm^{-1} (N—H stretching of neomycin) and around 1600 cm^{-1} (C═C stretching of neomycin), confirming the successful entrapment of drug in lignin-chitosan film. DSC thermograms (Fig. 3b) showed endothermic peak from 263 to 288.64 °C in neomycin sulphate corresponding to its melting point. The endothermic peak in drug-loaded film shifted to higher temperature indicating the successful encapsulation of neomycin sulphate in the polymeric matrix of film. The variation of peak position is probably due to the physical and molecular changes as a result of interactions between the polymers and drug [9].

4.3. In-vitro drug release studies

The slow drug release in a time-dependent manner was observed from polymeric film in 8 h, with cumulative release of 83.76 and 97.94 % for 5 and 10 mg/mL drug, respectively. However, film with 15 mg/mL of drug showed saturation at 7 h with 58.2 % release followed by slow release. Based on drug release profile, the film with 10 mg/mL drug was selected for further evaluation. The release kinetics showed that the film followed Weibull_4 model with sigmoidal release.

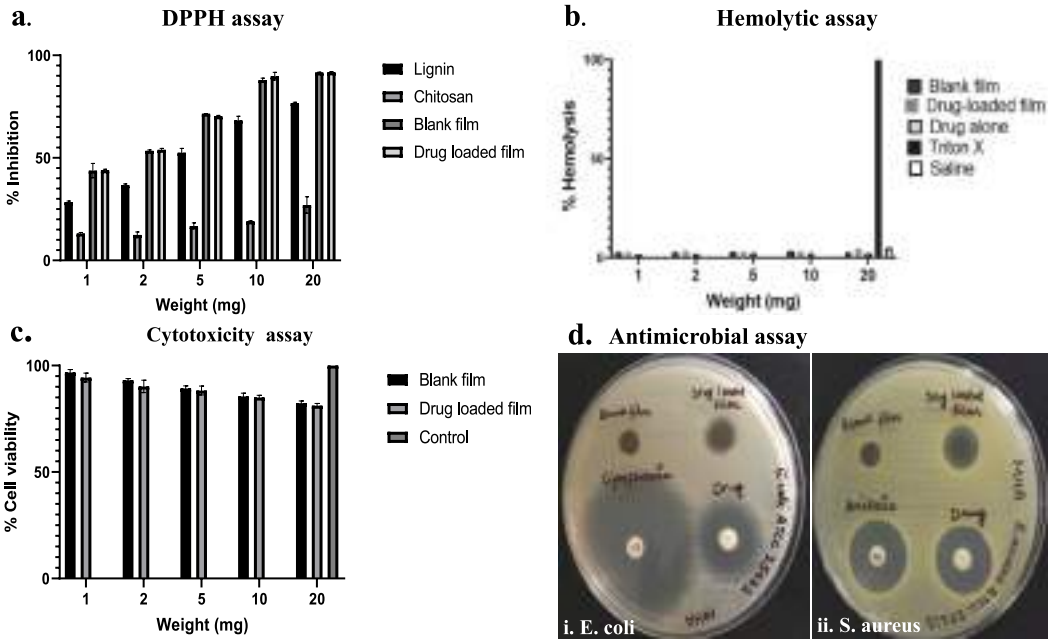

Fig. 4. a. DPPH assay b. Hemolytic assay c. Cytotoxicity assay d. Antimicrobial assay.

4.4. DPPH assay

DPPH was used to assess the free radical scavenging potential and at the highest quantity i.e. 20 mg, radical-scavenging activity was found to be 76 %, 27 %, 91.61 % & 91.67 % for lignin, chitosan, blank film & drug-loaded film, respectively (Fig. 4a). Antioxidant activity can be attributed to the presence of aromatic rings and multifunctional groups in lignin [10] and hydroxyl and amino groups in chitosan as reported previously [4].

4.5. Hemotoxicity

The formulation should be hemocompatible for safe application. As per literature, % hemolysis < 10 % is considered to be non-hemolytic [5]. No hemolytic activity was observed in any of the samples tested (Fig. 4b), thus can be considered safe for application.

4.6. Cytotoxicity

Different quantities of samples were evaluated for cell viability in McCoy fibroblast cell line using MTT assay (Fig. 4c). Both blank and drug-loaded films showed cell viability > 80 % hence, can be considered non-toxic and safe for use [6].

4.7. Antimicrobial activity

In the antimicrobial assay, the zones of growth inhibition against *E. coli* were 18 ± 1 and 11 ± 1 mm (Mean $\pm$ SD) for drug-only control and drug-loaded film, respectively. Likewise, the mean zones against *S. aureus* were 20 ± 1 and 13 ± 1 mm (Mean $\pm$ SD) for drug-only control and drug-loaded film, respectively. Thus, the drug-loaded film demonstrated effective bacterial inhibition against both bacteria whereas no activity was seen in blank film (Fig. 4d). The activity of neomycin alone was comparatively higher than the drug-loaded film which can be attributed to slow concentration-dependent release of drug from polymeric matrix as opposed to fast direct interaction with free drug [9].

5. Conclusion

Biocomposite polymeric film was prepared with 1:5 (lignin:chitosan) ratio using oven-drying method. The prepared films were further optimized by varying the drug concentration and were evaluated for their physicochemical and drug-release characteristics. Homogenous films with uniform surface and fibrous nature were observed. The film exhibited slow drug release with cumulative release of 97.94 % in 8 h and it follows Weibull_4 order release kinetics. The films were non-hemolytic and non-toxic towards fibroblast cells and showed excellent anti-oxidant activity. Furthermore, the drug-loaded film was active against both Gram-negative and Gram-positive bacteria seen in common skin and wound infections. Overall, the developed lignin-chitosan film showed excellent characteristics and can be employed for loading antibacterial drugs for topical applications and holds great promise for clinical translation.

CRediT authorship contribution statement

Pritiman Pothal: Investigation, Writing – original draft, Methodology. **Khushboo Pathania:** Investigation, Writing – original draft, Methodology, Validation. **Sunil Kumar:** Resources, Writing – review & editing. **Jasdeep Kaur:** Resources. **Sangeeta P. Sah:** Resources, Writing – review & editing. **Rachna Singh:** Conceptualization, Writing – review & editing. **Sandip V. Pawar:** Conceptualization, Supervision, Project administration, Writing – original draft, Writing – review & editing, Funding acquisition.

Declaration of Competing Interest

The authors declare that they have no known competing financial interests or personal relationships that could have appeared to influence the work reported in this paper.

Data availability

Data will be made available on request.

Acknowledgments

SVP acknowledge financial support from UGC, New Delhi, India for Start-up grant No.F.4-5(65-FRP) (lv-cycle)/201 7(BSR). KP is grateful to CSIR for JRF [File No: 09/0135(13255)/2022-EMRI].

References

[1] R. Nadányi, A. Ház, A. Lisý, M. Jablonský, I. Šurina, V. Majová, A. Baco, Lignin modifications, applications, and possible market prices, Energies 15 (2022) 1–16, https://doi.org/10.3390/en15186520.

[2] S. Alven, B.A. Aderibigbe, Chitosan and cellulose-based hydrogels for wound management, Int. J. Mol. Sci. 21 (2020) 1–30, https://doi.org/10.3390/ijms21249656.

[3] S.R. Yearla, K. Padmasree, Preparation and characterisation of lignin nanoparticles: evaluation of their potential as antioxidants and UV protectants, J. Exp. Nanosci. 11 (2016) 289–302, https://doi.org/10.1080/17458080.2015.1055842.

[4] A. Aradmehr, V. Javanbakht, A novel biofilm based on lignocellulosic compounds and chitosan modified with silver nanoparticles with multifunctional properties: synthesis and characterization, Colloids Surf. A 600 (2020), 124952, https://doi.org/10.1016/j.colsurfa.2020.124952.

[5] K. Amin, R. Dannenfelser, In vitro hemolysis : guidance for the pharmaceutical scientist, J. Pharm. Sci. 95 (2006) 1173–1176, https://doi.org/10.1002/jps.

[6] J. López-García, M. Lehocký, P. Humpolíček, P. Sáha, HaCaT keratinocytes response on antimicrobial atelocollagen substrates: extent of cytotoxicity, cell viability and proliferation, J. Funct. Biomater. 5 (2014) 43–57, https://doi.org/10.3390/jfb5020043.

[7] M. Weinstein, M100 Performance Standards for Antimicrobial Susceptibility Testing, 2021.

[8] K. Crouvisier-Urion, P.R. Bodart, P. Winckler, J. Raya, R.D. Gougeon, P. Cayot, S. Domenek, F. Debeaufort, T. Karbowiak, Biobased composite films from chitosan and lignin: antioxidant activity related to structure and moisture, ACS Sustain. Chem. Eng. 4 (2016) 6371–6381, https://doi.org/10.1021/acssuschemeng.6b00956.

[9] I.P. Merlusca, D.S. Matiut, G. Lisa, M. Silion, L. Gradinaru, S. Oprea, I.M. Popa, Preparation and characterization of chitosan–poly(vinyl alcohol)–neomycin sulfate films, Polym. Bull. 75 (2018) 3971–3986, https://doi.org/10.1007/s00289-017-2246-1.

[10] Z. Qin, H. Liu, L. Gu, R. Sun, X. Wang, Reactive and functional polymers volume one, React. Funct. Polym. Vol. One (2020), https://doi.org/10.1007/978-3-030-43403-8.